

1 The Role of Ice Nuclei Recycling in the Maintenance of Cloud Ice in
2 Arctic Mixed-Phase Stratocumulus

3 Amy Solomon¹², Graham Feingold², and Matthew D. Shupe¹²

4 (1) Cooperative Institute for Research in Environmental Sciences, University of Colorado
5 Boulder, Boulder, Colorado, USA.

6 (2) Earth System Research Laboratory, National Oceanic and Atmospheric Administration,
7 Boulder, Colorado, USA.

8

9 Corresponding author: Amy Solomon, NOAA/ESRL, PSD3, 325 Broadway, Boulder,
10 Colorado 80305-3337, USA. (amy.solomon@noaa.gov)

11 September 12, 2015

13 This study investigates the maintenance of cloud ice production in Arctic mixed phase
14 stratocumulus in large eddy simulations that include a prognostic ice nuclei (IN) formulation
15 and a diurnal cycle. Balances derived from a mixed-layer model and phase analyses are used
16 to provide insight into buffering mechanisms that maintain ice in these cloud systems. We
17 find that for the case under investigation, IN recycling through subcloud sublimation
18 considerably prolongs ice production over a multi-day integration. This effective source of
19 IN to the cloud dominates over mixing sources from above or below the cloud-driven mixed
20 layer. Competing feedbacks between dynamical mixing and recycling are found to slow the
21 rate of ice lost from the mixed layer when a diurnal cycle is simulated. The results of this
22 study have important implications for maintaining phase partitioning of cloud ice and liquid
23 that determine the radiative forcing of Arctic mixed-phase clouds.

24 **1 Introduction**

25 Reliable climate projections require realistic simulations of Arctic cloud feedbacks. Of
26 particular importance is accurately simulating Arctic mixed-phase stratocumuli (AMPS),
27 which are ubiquitous and play an important role in regional climate due to their impact on the
28 surface energy budget and atmospheric boundary layer structure through cloud-driven
29 turbulence, radiative forcing, and precipitation (Curry et al., 1992; Walsh and Chapman,
30 1998; Intrieri et al., 2002; Shupe and Intrieri, 2004; Sedlar et al., 2011; Persson, 2012). For
31 example, Bennartz et al. (2012) showed that the extreme melt events observed at Summit,
32 Greenland in July 2012 would not have occurred without the surface radiative forcing
33 produced by AMPS.

34 AMPS are characterized by a liquid cloud layer with ice crystals that precipitate from cloud
35 base even at temperatures well below freezing (Hobbs and Rangno, 1998; Intrieri et al.,
36 2002; McFarquhar et al., 2007). Radiative cooling near cloud top generates turbulence that
37 maintains the liquid layer and forms an approximately well-mixed layer that extends as far as
38 500 meters below cloud base. These cloud-driven mixed layers are frequently decoupled
39 from the surface layer, limiting the impact of fluxes of heat, moisture, and aerosols on the
40 cloud layer from below (Solomon et al., 2011; Shupe et al., 2013). However, unlike
41 subtropical cloud-topped boundary layers where decoupling enhances cloud breakup by
42 cutting the cloud system off from the surface source of moisture, decoupled AMPS can
43 persist for extended periods of time due to weak precipitation fluxes out of the mixed layer
44 and relatively moist air entrained into the cloud layer at cloud top (Tjernström et al., 2004;
45 Solomon et al., 2011; Sedlar et al., 2012; Solomon et al., 2014).

46 AMPS are challenging to model due to uncertainties in ice microphysical processes that
47 determine phase partitioning between ice and radiatively important cloud liquid water
48 (Sandvik et al., 2007; Tjernström et al., 2008; Klein et al., 2009; Karlsson and Svensson,
49 2011; Barton et al., 2012; Birch et al., 2012; de Boer et al., 2012), which drives turbulence
50 that maintains the system. Phase partitioning depends upon the number, shape, and size of ice
51 crystals, since these determine the efficiency of water vapor uptake by ice and hence the
52 availability of water vapor for droplet formation (Chen and Lamb, 1994; Sheridan et al.,
53 2009; Ervens et al., 2011; Hoose and Möhler, 2012).

54 Since temperatures in AMPS are too warm for homogenous ice nucleation, ice must form
55 through heterogeneous nucleation. Aerosols with properties to serve as seeds for
56 heterogeneous ice crystal formation are referred to as ice nuclei (IN). A number of different
57 aerosols such as mineral dust (Broadley et al., 2012; Kulkarni et al., 2012; Lüönd et al., 2010;
58 Möhler et al. 2006; Pinti et al., 2012; Welti et al., 2009), soot (DeMott, 1990), sea salts (Wise
59 et al., 2012), and bacteria (Kanji et al., 2011; Levin and Yankofsky, 1983) have been
60 observed to act as IN, all of which nucleate at different temperatures and supersaturation
61 ranges. In addition, observations indicate that nucleation properties are modified by aging
62 and coating of aerosols (Möhler et al., 2005; Cziczo et al. 2009). Heterogeneous ice
63 nucleation can occur by a number of modes: either in the presence of super-cooled droplets,
64 when an aerosol comes into contact with a droplet (contact freezing), is immersed in a
65 droplet (immersion freezing), or by vapor deposition on IN (deposition freezing) (Pruppacher
66 and Klett, 1997).

IN can be entrained into the cloud-driven mixed layer through turbulent mixing from above and/or below. Recent studies indicate that entrainment alone cannot account for observed ice crystal number concentration (N_{ICE}) (Fridlind et al., 2012), motivating the use of diagnostic formulations for ice formation to produce model simulations of AMPS with realistic phase partitioning (Ovchinnikov et al., 2011). While this modeling strategy constrains N_{ICE} to be close to the measured values it eliminates the dynamical-microphysical feedbacks that regulate ice/liquid phase partitioning (Avramov et al., 2011).

Here we investigate a relatively unexplored source of ice production--recycling of ice nuclei in regions of ice subsaturation. AMPS frequently have ice-subsaturated air near the cloud-driven mixed-layer base where falling ice crystals can sublimate, leaving behind IN. This feedback loop is referred to hereon as “recycling”. Recycling was found to be significant in large eddy simulations of a single-layer stratocumulus observed during the Department of Energy Atmospheric Radiation Measurement Program’s Mixed-Phase Arctic Cloud Experiment (M-PACE; Verlinde et al., 2007; Fan et al., 2009). AMPS observed during M-PACE formed due to a cold-air outbreak, where large fluxes of heat and moisture over the open ocean forced turbulent roll clouds that were coupled to the surface layer. This coupling with the surface layer prevented the identification of the role of dynamics internal to the cloud-driven mixed layer in maintaining phase-partitioning.

In this study we focus on the internal microphysics and dynamics of the cloud-driven mixed layer by investigating processes in an AMPS decoupled from surface sources of moisture, heat, and ice nuclei. We posit that recycling plays a significant role more generally since, for example, assuming an adiabatic vertical profile, a 650 meter-deep mixed layer with a cloud-

top temperature of -16°C requires a water vapor mixing ratio of at least 1.7 g kg^{-1} at mixed-layer base to be saturated with respect to ice, i.e., in order for recycling to be a *negligible* source of ice nuclei in the mixed layer. This value is typically only seen in the Arctic between May-September (Serreze et al., 2012), while persistent AMPS frequently occur outside of these months (Shupe et al., 2011).

We examine the role of IN recycling in maintaining ice production using large eddy simulations of a springtime decoupled AMPS. Three simulations are analyzed; a “Control” with recycling turned on and shortwave radiation turned off (to compare with previous simulations of this case that use different IN formulations and shortwave radiation turned off), “NoRecycle” with IN recycling turned off to identify the impact of recycling on the cloud life-time and phase partitioning, and “SW” with recycling and shortwave radiation turned on to identify the impact of realistic diurnal heating and cooling tendencies on the recycling process. This study builds on previous studies of this case, all of which exclude shortwave radiation (Avramov et al., 2011; Solomon et al., 2011, 2014), by including a prognostic equation for IN and a diurnal cycle. Within this modeling framework we investigate the relative roles of recycling and entrainment of IN in maintaining cloud ice production.

2 Case Description

The case derives from observations of a persistent single-layer Arctic mixed-phase stratocumulus cloud observed near Barrow, AK on 8 April 2008 during the Indirect and Semi-Direct Aerosol Campaign (McFarquhar et al., 2011) (see Fig. 1). The adjacent Beaufort Sea was generally ice covered during this time, with significant areas of open water observed east of Barrow. A 4-K temperature inversion with inversion base at 1.05 km was observed

111 via a radiosonde at 17:34UTC; static stability was near neutral within the mixed layer
112 overlaying a stable near-surface layer with static stability greater than 2 K km^{-1} below 500 m.
113 The water vapor mixing ratio, q_v , decreased from 1.7 g kg^{-1} at the surface to 1.2 g kg^{-1} at
114 cloud top, above which a secondary maximum of 1.6 g kg^{-1} was observed. Winds were east-
115 southeasterly throughout the lowest 2 km.

116 Measurements from ground-based, vertically pointing, 35-GHz cloud radar, micropulse lidar,
117 and dual-channel microwave radiometer at Barrow indicated a mixed-phase cloud layer
118 starting at 8 UTC on 8 April 2008 with a cloud top at approximately 1.5km that slowly
119 descended to approximately 0.5 km over a 26 hour period. At the time of the 17:34 sounding
120 the cloud layer extended into the inversion by 100 m, had a cloud base at 0.9 km, and cloud
121 top at 1.15 km. Cloud ice water path (IWP), derived from cloud radar reflectivity
122 measurements, varied from $20\text{--}120 \text{ g m}^{-2}$ within 10 min of the sounding, with an uncertainty
123 of up to a factor of 2 (Shupe et al., 2006). Concurrently liquid water path (LWP), derived
124 from dual-channel microwave radiometer measurements, was $39\text{--}62 \text{ g m}^{-2}$, with an
125 uncertainty of $20\text{--}30 \text{ g m}^{-2}$ (Turner et al., 2007).

126 Research flights were conducted by the National Research Council of Canada Convair-580 at
127 22:27-23:00 UTC on 8 April 2008 over the ocean northwest of Barrow (McFarquhar et al.,
128 2011). Droplet concentrations measured by a Particle Measuring Systems Forward Scattering
129 Spectrometer Probe varied between 100 and 200 cm^{-3} . Ice crystal number concentrations
130 measured by Stratton Park Engineering Company 2D-S and Particle Measuring Systems 2D-
131 P optical array probes for sizes larger than $100 \text{ }\mu\text{m}$ together averaged 0.4 L^{-1} . IN
132 concentrations measured with the Texas A&M Continuous Flow Diffusion Chamber varied

from 0.1 L^{-1} to above 20 L^{-1} . Ice crystal habit estimated using the automated habit classification procedure of Korolev and Sussman (2000) indicated primarily dendritic crystal habits.

3 Model Description

We use the large eddy simulation mode of the Advanced Research WRF model (WRFLES) Version 3.3.1 (Yamaguchi and Feingold, 2012) with the National Center for Atmospheric Research Community Atmospheric Model longwave radiation package (Collins et al., 2004), RRTMG shortwave package (Iacono et al., 2008), the Morrison two-moment microphysical scheme (Morrison et al., 2009), and a 1.5-order turbulent kinetic energy prediction scheme (Skamarock et al., 2008). Surface fluxes are calculated using the modified MM5 similarity scheme which calculates surface exchange coefficients for heat, moisture, and momentum following Webb (1970) and uses Monin-Obukhov with Carlson-Boland viscous sub-layer and standard similarity functions following Paulson (1970) and Dyer and Hicks (1970).

All model runs are initialized with winds, temperature, and water vapor from the 17Z 8 April 2008 sounding at Barrow, AK (see Fig.1). Initial surface pressure is 1020 hPa. Divergence is assumed to be $2.5 \times 10^{-6} \text{ s}^{-1}$ below the temperature inversion and zero above, giving a linear increase in large-scale subsidence from zero at the surface to 2.7 mm s^{-1} at the base of the initial inversion ($z=1.1 \text{ km}$). This value for divergence was chosen so that the height of the temperature inversion at cloud top is steady. The divergence used in this study is smaller than the divergence used in the WRFLES study of the same case by Solomon et al. (2014) due to

the reduced LWPs in this current study and therefore reduced turbulent entrainment that balances large-scale subsidence in a steady simulation.

All simulations are run on a domain of $3.2 \times 3.2 \times 1.8$ km with a horizontal grid spacing of 50 m and vertical spacing of 10 m. The domain has $65(x) \times 65(y) \times 180(z)$ gridpoints and is periodic in both the x- and y-directions. The top of the domain is at 1.8 km, which is 0.7 km above cloud top in this case. The model time step is 0.75 s. The structure of the cloud layer is insensitive to changes in resolution and domain size. For example, tests run for Solomon et al. (2014) demonstrated that increasing the vertical and horizontal resolutions by a factor of two resulted in an increase in LWP and IWP by 5% and 1%, respectively, while increasing the domain size by a factor of two in both the x- and y-directions results in an increase in LWP and IWP of less than 1%.

Cloud droplets are activated using resolved and subgrid vertical motion (Morrison and Pinto 2005) and a log-normal aerosol size distribution (assumed to be ammonium bisulfate and 30% insoluble by volume) to derive cloud condensation nuclei spectra following Abdul-Razzak and Ghan (2000). The aerosol accumulation mode is specified with concentrations of 165 cm^{-3} , modal diameter of $0.2 \text{ }\mu\text{m}$, and geometric standard deviation of $1.4 \text{ }\mu\text{m}$, based on in situ ISDAC measurements. In this formulation, IN and cloud condensation nuclei are treated as separate species.

Temperature and moisture profiles are nudged to the initial profiles in the top 400 m of the domain with a time scale of 1 hour. The model is initialized with winds, temperature, and water vapor similar to the Control integration from Solomon et al. (2014). Horizontal winds

174 are nudged to the initial profiles at and above the initial inversion base with a timescale of 2
175 hours. Initial temperature and subgrid turbulent kinetic energy (TKE) are perturbed below the
176 top of the mixed layer with pseudo-random fluctuations with amplitudes of +/- 0.1 K and 0.1
177 $\text{m}^2 \text{s}^{-2}$, respectively. The liquid layer is allowed to form in the absence of ice during the first
178 hour of the integration to prevent potential glaciation during spinup.

179 The cloud-driven mixed layer is defined as the region where the liquid-ice water static energy
180 is approximately constant with height. We define the boundaries of the mixed-layer top and
181 base to occur where the slopes of liquid-ice static energy exceed $7 \times 10^{-3} \text{ K m}^{-1}$ and $1 \times 10^{-3} \text{ K}$
182 m^{-1} , respectively. Cloud top and base are defined as the heights where cloud water mixing
183 ratio, q_c , is equal to $1 \times 10^{-4} \text{ g kg}^{-1}$.

184 Nested Weather Research and Forecasting (WRF) model simulations of this case performed
185 with an inner grid at LES resolution (Solomon et al. 2011) demonstrate that moisture is
186 provided to the cloud system by a total water inversion at cloud top and that the mixed layer
187 does not extend to the surface, i.e., the mixed layer is largely decoupled from surface sources
188 of moisture. In addition, the nested simulations indicate that cloud liquid water, q_c , is
189 maintained within the temperature inversion by downgradient turbulent fluxes of q_v from
190 above and direct condensation driven by radiative cooling. These processes cause at least
191 20% of q_c to extend into the temperature inversion.

192 WRFLES has been modified to include a prognostic equation for IN number concentration
193 (N_{IN}),

$$\frac{\partial N_{IN}}{\partial t} + ADV + DIFF = \left. \frac{\delta N_{IN}}{\delta t} \right|_{activation} + \left. \frac{\delta N_{IN}}{\delta t} \right|_{sublimation} \quad (1)$$

194 where ADV represents advection and DIFF represents turbulent diffusion. Activation is also
 195 referred to as nucleation of ice and sublimation is also referred to as recycling of IN.

196 Here we adopt an empirical approach by initializing N_{IN} with an observationally based
 197 relationship expressing the number of available IN as a function of temperature in regions of
 198 water-saturation (DeMott et al., 2010),

$$N_{IN} = F * 0.117 \exp(-0.125 * (T - 273.2)) \quad (2)$$

199 where F is an empirically derived scale factor and T is temperature in Kelvin. Sixteen
 200 prognostic equations are integrated for N_{IN} in equally spaced temperature intervals with
 201 nucleation thresholds between -20.2°C and -15.5°C (see Fig. 2). Therefore, additional IN
 202 become available for activation with decreasing temperature and as the cloud layer cools. IN
 203 number concentrations are initially specified using equation 2, such that the initial IN in bin k
 204 is equal to the number of IN calculated by equation 2 at the threshold temperature $k + 1$
 205 minus that calculated at temperature k . After the initial time 50% of the IN available in a bin
 206 nucleates if the in-situ temperature is above the threshold temperature and the local
 207 conditions exceed water saturation. Therefore, initial N_{IN} concentrations are a function of the
 208 nucleation threshold temperatures and are independent of the in-situ temperature. The in-situ
 209 temperature in regions of water saturation determines how many IN are activated. Due to the
 210 pristine dendritic nature of the observed crystals, ice shattering and aggregation are neglected
 211 in the simulations and sublimation returns one N_{IN} per crystal.

212 N_{IN} (in units of L^{-1}) integrated over the domain in each temperature bin k at time t is equal to

$$\bar{N}_{IN}(k, t) = \iiint N_{IN}(x, y, z, k, t) \, dx \, dy \, dz. \quad (3)$$

213 Upon sublimation, the modification of activation thresholds that can occur for previously
214 nucleated IN, i.e. preactivation (Roberts and Hallett, 1967), is not considered and N_{IN} are
215 returned to each bin k with weighting

$$W_k = [\bar{N}_{IN}(k, 0) - \bar{N}_{IN}(k, t)] / \bar{N}_{IN}(k, 0) \quad (4)$$

216 where W_k is normalized such that $\sum W_k = 1$. The W_k are recalculated each time step. In this
217 way, IN are recycled preferentially to each of the 16 temperature bins from which they
218 originated (Feingold et al., 1996).

219 The factor F in Eq. (2) is set to 4 for all simulations yielding an initial N_{IN} summed over all
220 bins at every gridpoint equal to $5.8 \, L^{-1}$, compared to $10 \, L^{-1}$ used in LES studies of the same
221 case presented in Avramov et al. (2011). In a discrete bin formulation this results in $3.26 \, L^{-1}$
222 in the warmest bin and $0.23 \, L^{-1}$ additional IN that are available for nucleation in the coldest
223 bin, resulting in N_{IN} given by eq. (2) evaluated at the temperature the coldest bin (-20.2°C).
224 Given the initial temperatures in the cloud layer, all IN from the first bin in the cloud layer
225 nucleate. This causes an initial spike in cloud ice number concentration, which also causes a
226 large precipitation flux out of the mixed layer. It takes approximately 6 hours for the cloud
227 layer to reach a quasi-equilibrium with steady cloud ice production. Supplementary
228 integrations were done to test for robustness of the results presented in Section 4 by varying
229 initial IN concentrations, i.e., the factor F , (shown in Fig. 3) and by varying snow density and

230 fall speeds (shown in Fig. 4). Fig. 3 shows that the simulation maintains ice production when
231 the initial N_{IN} is increased or decreased by $\sim 3 \text{ L}^{-1}$ relative to Control. Fig. 4 shows that the
232 simulations maintain quasi-steady ice and liquid water paths after an initial spinup but the
233 amount of ice produced is sensitive to the snow fall speed.

234 Crystal size distributions for averaged values of ice water mixing ratio and number
235 concentration from the Control integration are shown in Fig. 5. These crystal size
236 distributions are consistent with the Avramov et al. (2011) simulations of this case where
237 crystal habits are assumed to be high-density pristine dendrites. The distribution shown in Fig.
238 5 underestimates the number of large (greater than 5mm) crystals as estimated by the 2D-S
239 and 2D-P probes (see Avramov et al. (2011) for a detailed discussion of the measurements).

240 The Control integration is run with shortwave radiation turned off in order to compare with
241 previous LES studies of this case (Avramov et al. 2011; Solomon et al. 2014). The results of
242 Control are compared to two additional simulations; one with IN recycling turned off
243 (hereafter “NoRecycle”) and one with recycling and shortwave radiation both turned on
244 (hereafter “SW”). SW is used to investigate how the diurnal cycle impacts IN recycling and
245 ice formation. All runs use the same setup except SW has subsidence reduced by 30% to
246 keep the mixed-layer top from lowering appreciably because of smaller LWPs. This allows
247 for direct comparisons of mixed layer structure and fluxes at the mixed layer boundaries. The
248 NoRecycle run is started from the Control run at hour 6 to prevent the two simulations from
249 diverging due to spinup. The first six hours of integration are not used in the analysis to allow
250 for the spinup of cloud ice. Hours 6-40 are used for analysis of the Control and NoRecycle

simulations and hours 16-76 are used for analysis of the SW simulation to allow for multiple diurnal cycles.

4 Model Results

4.1 Control Integration

In the quasi-steady Control integration, the mixed-layer depth is approximately 850 m and comprises a 375 m deep mixed-phase cloud layer (henceforth “the cloud layer”), extending above the mixed-layer top by 25 m, and a 500 m subcloud layer below (Fig. 6). IN are produced by sublimation of ice crystals below the cloud layer, advected to the cloud layer by turbulence, and activated as ice crystals (Fig. 6). Ice that forms in the cloud layer is transported vertically by turbulence, precipitates to cloud base and below, and sublimates below the cloud layer. At the mixed-layer base, an increase in N_{ICE} due to precipitation approximately balances a decrease in N_{ICE} due to sublimation. These processes constitute a feedback through which ice production and IN recycling are closely related. This feedback between ice production and IN in the mixed layer is linked to dynamic-thermodynamic tendencies, which sustain a subsaturated subcloud layer because the decrease in relative humidity due to an upward turbulent vapor flux exceeds the increase due to sublimation.

The time evolution of horizontally-averaged IN advection plus subsidence (Fig. 7a) shows that the majority of IN activate at cloud base, which is a bit warmer than cloud top but is sufficiently cold to activate many of the IN. However, IN from bins with colder threshold temperatures are advected higher into the cloud where they activate at their threshold temperature. A secondary maximum is seen at cloud top where the coldest temperatures are

272 found. Also, it is seen that IN are advected into the cloud layer at cloud top for the first 15-18
273 hours, but this source of IN decreases as IN in the upper entrainment zone are depleted. The
274 turbulent mixing of snow and ice in the mixed-phase cloud layer is clearly seen in Fig. 7b,
275 where ice plus snow number concentrations are well-mixed in the cloud layer. Given the
276 efficient mixing by the turbulent eddies, it is not possible to identify whether ice has
277 nucleated at cloud base or cloud top from the ice number concentrations alone. Fig. 7 also
278 shows the time-height cross sections of horizontally-averaged water vapor mixing ratio and
279 relative humidity with respect to ice. These figures show that the continuous drying and
280 cooling of the mixed layer results in continuous sublimation in the subcloud layer.

281 LWP and IWP remain steady until hour 16 of the simulation, and decrease slowly thereafter
282 (solid lines in Fig. 8a). LWP and IWP magnitudes are within the observational estimates for
283 this case. In addition, the cloud system is sustained over a multi-day period similar to
284 measurements taken during ISDAC. Continuous cloud-top cooling causes the minimum
285 horizontally-averaged temperature (near cloud top) to decrease from -17.5°C to -20°C from
286 hour 10 to hour 40 (Fig. 8b).

287 Over the 40-hour integration, the mixed layer remains decoupled from the surface (Fig. 8c).
288 However, this does not prevent the number concentration of ice crystals (N_{ICE}) in the cloud
289 layer from remaining relatively steady, decreasing from vertically integrated values of 372 to
290 365 m L^{-1} (Fig. 8d, or in terms of vertically averaged cloud layer values, 1.2 L^{-1} to 1.1 L^{-1}).
291 By contrast, while N_{ICE} is maintained in the cloud layer, N_{IN} in the subcloud layer decreases
292 significantly from 2 L^{-1} to 0.2 L^{-1} over the same period. Therefore, even though more N_{ICE}
293 are lost from the cloud than are activated (Fig. 9a), the relatively constant flux of IN into the

cloud layer (Fig. 9b) allows N_{ICE} in the cloud to decrease at a slower rate than N_{IN} in the subcloud layer. The continuous loss of N_{IN} in the subcloud layer is due to the IN flux into the cloud layer exceeding the N_{IN} gained through sublimation and turbulent advection at mixed-layer base (Fig. 9b). This loss is not mitigated by entrainment at mixed-layer top, which is found to be negligible (Fig. 9c), consistent with Fridlind et al. (2011).

The feedback loops discussed above are illustrated by the conceptual diagram in Fig. 10, where any change to one link in the cycle leads to an increase or decrease in ice production. For example, a decrease in the turbulent advection of N_{IN} into the cloud layer, slows the activation of IN, reduces the precipitation flux into the subcloud layer, reducing sublimation and availability of IN below cloud base. Both dynamics and thermodynamics play a role in the buffering aspect of these feedback loops since, for example, the slowing of IN activation in the example above would lead to increased cloud liquid production, cloud-top radiative cooling, and enhanced turbulent mixing, which would lead to increased transport of IN into the cloud layer and therefore increased activation of IN.

4.2 Impact of turning off recycling

When IN recycling is turned off, all IN that activate are lost from the system. This results in a more rapid loss of IN, a decrease in IWP, and a rapid increase in LWP (Fig. 8a,d, dashed lines), in contrast to the measurements that show a steady liquid layer and consistent ice production. Increased cloud liquid water when recycling is turned off results in increased radiative cooling at cloud top, which causes the cloud-driven mixed layer to cool more rapidly (Fig. 8b). These results demonstrate the importance of IN recycling in regulating

phase partitioning. The rapid increase in LWP increases cloud-generated turbulence via enhanced radiative cooling and increases the turbulent mixing of IN from the subcloud layer into the cloud layer, contributing to a more rapid depletion of IN relative to the Control integration. This process eventually becomes limited due to depletion of IN in the reservoir below (Fig. 9b). Due to the additional activation of IN as the cloud layer cools, ice production is maintained in the absence of recycling and the activation of IN in the cloud layer exceeds the upward IN flux at cloud base (Fig. 9a,b). However, the diminishing N_{IN} in the subcloud layer limits IN activation and N_{ICE} rapidly decreases in the cloud layer (Fig. 8d).

4.3 Impact of diurnal cycle

A diurnal cycle is added to the Control simulation in order to investigate how the feedback loops identified in the Control and NoRecycle runs are modified with realistic transient heating and cooling tendencies due to variations in incoming shortwave radiation. A question that is addressed in this diurnal simulation is, to what extent is the continuous production of ice in the Control simulation due to the lack of incoming shortwave radiation, which may overestimate the cooling tendencies in the cloud layer, resulting in an overestimate of IN activation? In addition, we investigate whether allowing for a realistic diurnal cycle provides for additional negative or “buffering” feedbacks.

Adding a diurnal cycle to the Control simulation produces a diurnal peak in downwelling surface shortwave radiation of 510 W m^{-2} and 6 hours of total darkness per day (Fig. 11b). As shortwave radiation increases, the net radiative cooling near cloud top diminishes, which decreases cloud-generated turbulence, decreasing LWP and cloud-layer thickness. In addition,

it is seen that the peak daily LWP coincides with zero shortwave radiation when in-cloud turbulence and cloud thickness are largest (Fig. 11a). These values are on the low end but within the measurements for this ISDAC case.

Fig. 11a,b shows that LWP and IWP variability is predominantly driven by the diurnal cycle. However, IWP variability is seen to lag LWP by 3-4 hours because as shortwave radiation decreases the cloud layer cools, which increases activation of IN, increasing N_{ICE} , allowing more ice crystals to grow, which increases IWP (Fig. 11a,b). Similar to the Control simulation subcloud N_{IN} decreases at a faster rate than cloud layer N_{ICE} , but allowing for the warming and cooling tendencies in the diurnal cycle results in cloud layer N_{ICE} that decreases 40% more slowly than in the Control simulation (Fig. 11c).

Precipitation and turbulent mixing of N_{ICE} (hereafter turbulent mixing is referred to as “ T_{ICE} ”) at cloud base are out of phase by 10 hours (Fig. 11d), with turbulence leading precipitation. When shortwave radiation is weak or absent, the increase in N_{ICE} eventually becomes limited by a decreasing turbulent mixing of IN (“ T_{IN} ”) into the cloud layer from below, as recycling slows due to a decrease in N_{ICE} flux from the cloud layer (Fig. 11d,f). When shortwave radiation is strong, reduction in IWP is limited by weaker precipitation losses, and attendant weaker sublimation and IN flux into the cloud layer (Fig. 11d,f). Entrainment of N_{IN} at the mixed-layer top is insignificant throughout the integration (Fig. 11e).

5 Analysis from a mixed-layer perspective

356 The results discussed in Section 4 can be understood from balances in a well-mixed layer
 357 with sources/sinks at the upper and lower boundaries. Total particle concentration
 358 ($N_{IN}+N_{ICE}$) is only changed by fluxes at the mixed-layer boundaries when recycling is
 359 allowed. These fluxes are entrainment of N_{IN} at mixed-layer top and turbulent mixing of both
 360 N_{ICE} and N_{IN} (T_{ICE} and T_{IN}) and precipitation of N_{ICE} (P) at mixed-layer base. Since there
 361 are no sources and sinks of $N_{IN}+N_{ICE}$ within the mixed layer, the horizontally-averaged
 362 $N_{IN}+N_{ICE}$ flux ($f(z)$) must vary linearly from mixed-layer base to mixed-layer top (Lilly,
 363 1968; Bretherton and Wyant, 1997). If it is assumed that f at the mixed-layer base is
 364 downward (assumed negative in this formulation) and f at the mixed-layer top is negligible
 365 (robust assumptions for a scenario where ice is precipitating from the mixed layer and
 366 entrainment is weak), then

$$f(z) = R * \frac{H - z}{H - B}, \quad B \leq z \leq H \quad (5)$$

367 where H is the mixed-layer height, B is the mixed-layer base and R is the total $N_{IN}+N_{ICE}$ flux
 368 at the mixed-layer base,

$$R = f|_{\text{Mixed-Layer Base}} = [P + T_{ICE} + T_{IN}]_{\text{Mixed-Layer Base}}, \quad (6)$$

369 and

$$[T_{ICE} + T_{IN}]_{\text{Cloud Base}} \approx [f - P]_{\text{Cloud Base}}. \quad (7)$$

370 Since $f < 0$, the turbulent flux of N_{IN} into the cloud layer plus the turbulent flux of N_{ICE} into
 371 the subcloud layer is always less than precipitation of N_{ICE} at cloud base. In addition, in a

372 slowly evolving state where $T_{IN}|_{\text{Mixed-Layer Base}} > 0$, total IN flux due to sublimation in the
 373 mixed layer, S , can be written as

$$S \approx [P + T_{ICE}]_{\text{Mixed-Layer Base}} - [P + T_{ICE}]_{\text{Cloud Base}} \quad (8a)$$

$$374 \quad \approx [f - T_{IN}]_{\text{Mixed-Layer Base}} - [f - T_{IN}]_{\text{Cloud Base}} \quad (8b)$$

375 and since $f|_{\text{Mixed-Layer Base}}$ is downward and $f|_{\text{Mixed-Layer Top}}$ is negligible (eq. 5),

$$S < T_{IN}|_{\text{Cloud Base}} - T_{IN}|_{\text{Mixed-Layer Base}} \quad (8c)$$

$$< T_{IN}|_{\text{Cloud Base}}. \quad (8d)$$

376 Thus in a well-mixed layer with an upward $T_{IN}|_{\text{Mixed-Layer Base}}$, sublimation is always less than
 377 the flux of N_{IN} into the cloud layer.

378 Based on results from Control, precipitation of N_{ICE} at cloud base is sufficient to balance the
 379 upward turbulent flux of N_{IN} (i.e., $|T_{IN}| \gg |T_{ICE}|$ at cloud base). Therefore, in a well-mixed
 380 layer with precipitation of N_{ICE} at the mixed-layer base that is larger in magnitude than an
 381 upward turbulent N_{IN} flux at the mixed-layer base, and assuming negligible entrainment at
 382 the mixed-layer top

$$|P|_{\text{Cloud Base}} > T_{IN}|_{\text{Cloud Base}} > S. \quad (9)$$

383 However, if all N_{ICE} sublimate in the mixed layer and the upward turbulent flux of N_{IN}
 384 dominates at the mixed-layer base then $f > 0$ and

$$T_{IN}|_{\text{Cloud Base}} > |P|_{\text{Cloud Base}} = S, \quad (10)$$

385 the mixed layer gains $N_{IN} + N_{ICE}$ over time, resulting in a continuously increasing ice
 386 production in the cloud layer. In the presence of shortwave radiation (i.e., in the SW
 387 simulation), $T_{IN}|_{\text{Cloud Base}}$ is also greater than $|P|_{\text{Cloud Base}}$ after a period of weakened
 388 turbulence and weaker precipitation at the mixed-layer base, due to increased activation of
 389 N_{IN} due to decreasing shortwave radiation.

390 If IN entrainment at the mixed-layer top is not negligible then $f(z)$ must be modified to
 391 include fluxes at the mixed-layer top and $|f|_{\text{Cloud Base}}$ will increase. If $|f|_{\text{Cloud Base}}$ increases
 392 such that $f_{\text{Cloud Base}} < P_{\text{Mixed-Layer Base}}$, then sublimation will exceed $T_{IN}|_{\text{Cloud Base}}$.

393 This mixed-layer analysis provides a framework to understand the results presented in
 394 Section 4. Specifically, sublimation being less than the turbulent flux of IN is seen to be a
 395 property of a well-mixed layer where the total flux at mixed-layer base is downward and the
 396 total flux at the mixed-layer top is negligible. In the case where the mixed layer is saturated
 397 with respect to ice, sublimation is equal to zero and the turbulent flux of IN at the mixed-
 398 layer base is less than the turbulent flux of IN at the cloud base, reducing the flux of IN into
 399 the cloud layer. The relationships outlined in this section are appropriate for any AMPS with
 400 weak entrainment at cloud top, weak large-scale advective fluxes, and net downward fluxes
 401 at the mixed-layer base.

402 **6 Analysis of Buffered Feedbacks in SW**

403 Phase diagrams highlight the processes involved in ice production when a diurnal cycle is
 404 allowed (following the arrows from green to blue to black to red in Fig. 12a,b). When
 405 incoming shortwave radiation is a maximum, recycling (sublimation) is seen to be at a
 406 minimum. This is counterintuitive since subcloud relative humidity is low at this time, which
 407 would be expected to produce increased sublimation. However, due to weak turbulent mixing
 408 between the cloud and subcloud layers the net N_{ICE} flux into the subcloud layer is weak,
 409 resulting in weak sublimation and recycling. This situation is reversed as shortwave radiation
 410 decreases, since increased cloud-top cooling increases cloud-driven turbulent mixing, which
 411 allows recycling to increase in the regions of reduced subcloud relative humidity. As is seen
 412 in the conceptual diagram (Fig. 10), this then leads to an increased N_{ICE} flux into the
 413 subcloud layer (green arrows, Fig. 12). However, N_{ICE} in the cloud layer doesn't begin to
 414 increase until activation in the cloud layer exceeds the flux of N_{ICE} into the subcloud layer
 415 (green arrows). This cycle is further amplified as shortwave radiation decreases, namely,
 416 decreased shortwave radiation increases cloud-driven turbulence, increasing the flux of IN
 417 into the cloud layer, increasing the activation of IN, which increases N_{ICE} in the cloud layer
 418 and the N_{ICE} flux from the cloud layer into the subcloud layer (blue arrows).

419 When incoming shortwave radiation is a minimum, more N_{IN} are activated because the cloud
 420 layer cools. However, again we see that N_{ICE} tendencies due to thermodynamics are buffered
 421 by the slowing of turbulence-driven feedbacks due to a thickening of the cloud layer. Thus, a
 422 net increase in N_{ICE} in the cloud layer, commensurate with an increased IWP and
 423 precipitation (black arrows), is buffered by a decrease in the downward turbulent mixing of
 424 N_{ICE} , which reduces recycling, slowing the feedback loop (see Fig. 10). During the morning
 425 hours, as the cloud layer warms and thins and ice activation becomes less efficient,

turbulence continues to decline, slowing the recycling feedback process to the point where limited IN fluxes to the cloud layer inhibit ice production and N_{ICE} declines (red arrows).

7 Summary

We have demonstrated that sustained recycling of IN through a drying subcloud layer and additional activation of N_{IN} due to a cooling cloud layer are sufficient to maintain ice production, and regulate liquid production over multiple days in a decoupled AMPS.

This study provides an idealized framework to understand feedbacks between dynamics and microphysics that maintain phase-partitioning in AMPS. In addition, we have shown that modulation of the cooling of the cloud layer and the humidity of the subcloud layer by the diurnal cycle buffers the mixed-layer system from a loss of particles and promotes the persistence of a mixed-phase cloud system. The results of this study provide insight into the mechanisms and feedbacks that may maintain cloud ice in AMPS even when entrainment of IN at the mixed-layer boundaries is weak. While the balance of these processes changes depending upon the specific conditions of the cloud layer, for example whether the cloud layer is coupled to the surface layer, the mechanisms detailed in this paper will manifest to some degree and therefore the current study provides a framework for understanding the role of recycling in maintaining phase-partitioning in AMPS.

443 **Author Contributions:**

444 A.S., G.F., and M.D.S. conceived and designed the experiments; A.S. performed the
445 simulations; A.S., G.F., and M.D.S. analyzed the model results and co-wrote the paper.

446 **Acknowledgements:**

447 The authors acknowledge discussions with Alex Avramov, Chris Cox, Gijs de Boer, Barbara
448 Ervens, and Ann Fridlind, and Takanobu Yamaguchi for developing the software to run
449 WRF as a large eddy simulation. This research was supported by the Office of Science
450 (BER), U.S. Department of Energy (DE-SC0011918) and the National Science Foundation
451 (ARC-1023366).

References

- Abdul-Razzak, H. and Ghan, S. J.: A parameterization of aerosol activation 2. Multiple aerosol types, *J. Geophys. Res.*, 105, 6837–6844, 2000.
- Avramov, A., Ackerman, A. S., Fridlind, A. M., van Dierenhoven, B., Botta, G., Aydin, K., Verlinde, J., Korolev, A. V., Strapp, J. W., McFarquhar, G. M., Jackson, R., Brooks, S. D., Glen, A., and Wolde, M.: Toward ice formation closure in Arctic mixed-phase boundary layer clouds during ISDAC, *J. Geophys. Res.*, 116, D00T08, doi:10.1029/2011JD015910, 2011.
- Barton, N. P., Klein, S. A., Boyle, J. S., and Zhang, Y. Y.: Arctic synoptic regimes: Comparing domain wide Arctic cloud observations with CAM4 and CAM5 during similar dynamics, *J. Geophys. Res.*, 117, D15205, doi:10.1029/2012JD017589, 2012.
- Bennartz, R., Shupe, M., Turner, D., Walden, V., Steffen, K., Cox, C., Kulie, M. S., Miller, N., and Pettersen, C.: July 2012 Greenland melt extent enhanced by low-level liquid clouds, *Nature*, 496, 83-86, doi:10.1038/nature12002, 2012.
- Birch, C. E., Brooks, I. M., Tjernström, M., Shupe, M. D., Mauritsen, T., Sedlar, J., Lock, A. P., Earnshaw, P., Persson, P. O. G., Milton, S. F., and Leck, C.: Modeling atmospheric structure, cloud and their response to CCN in the central Arctic: ASCOS case studies, *Atmos. Chem. Phys.*, 12, 3419-3435, doi:10.5194/acp-12-3419-2012, 2012.
- Bretherton, C. S. and Wyant, M. C.: Moisture transport, lower-tropospheric stability, and decoupling of cloud-topped boundary layers, *J. Atmos. Sci.*, 54, 148-167, 1997.
- Broadley, S., Murray, B., Herbert, R., Atkinson, J., Dobbie, S., Malkin, T., Condcliffe, E., and Neve, L.: Immersion mode heterogeneous ice nucleation by an illite rich powder representative of atmospheric mineral dust, *Atmos. Chem. Phys.*, 12:287{307,

doi:10.5194/acp-12-287-2012, 2012.

Chen, J.-P. and Lamb, D.: The theoretical basis for the parameterization of ice crystal habits: Growth by vapor deposition, *J. Atmos. Sci.*, 51, 1206–1222, doi:10.1175/1520-0469(1994)051<1206:TTBFTP>2.0.CO;2, 1994.

Collins, W. D., Rasch, P. J., Boville, B. A., Hack, J. J., McCaa, J. R., Williamson, D. L., and Briegleb, B. P.: Description of the NCAR Community Atmosphere Model (CAM 3.0), NCAR Technical Note, NCAR/TN-464+STR, 226 pp., 2004.

Curry, J. and Ebert, E. E.: Annual cycle of radiation fluxes over the Arctic Ocean: Sensitivity to cloud optical properties, *J. Climate*, 5, 1267–1280, 1992.

Cziczo, D., Froyd, K., Gallavardin, S., Moehler, O., Benz, S., Saathoff, H., and Murphy, D.: Deactivation of ice nuclei due to atmospherically relevant surface coatings, *Environ. Res. Lett.*, 4:044013, doi:10.1088/1748-9326/4/4/044013, 2009.

de Boer, G., Chapman, W., Kay, J. E., Medeiros, B., Shupe, M. D., Vavrus, S., and Walsh, J.: A characterization of the present-day Arctic atmosphere in CCSM4, *J. Climate*, 25, 2676–2695, 2012.

DeMott, P. J.: An exploratory study of ice nucleation by soot aerosols, *J. Appl. Meteorol.*, 29(10), 1072–1079, 1990.

DeMott, P. J., Prenni, A. J., Liu, X., Petters, M. D., Twohy, C. H., Richardson, M. S., Eidhammer, T., Kreidenweis, S. M., and Rogers, D. C.: Predicting global atmospheric ice nuclei distributions and their impacts on climate, *P. Natl. Acad. Sci. USA*, 107, 11217–11222, doi:10.1073/pnas.0910818107, 2010.

Dyer, A. J. and Hicks, B. B.: Flux-gradient relationships in the constant flux layer, *Q. J. Roy. Meteor. Soc.*, 96, 715–721, 1970.

498 Ervens, B., Feingold, G., Sulia, K., and Harrington, J.: The impact of microphysical
 499 parameters, ice nucleation mode, and habit growth on the ice/liquid partitioning in
 500 mixed-phase Arctic clouds, *J. Geophys. Res.*, 116, D17205,
 501 doi:10.1029/2011JD015729, 2011.

502 Fan, J., Ovchinnikov, M., Comstock, J. M., McFarlane, S. A., and Khain, A.: Ice formation
 503 in Arctic mixed-phase clouds: Insights from a 3-D cloud-resolving model with size-
 504 resolved aerosol and cloud microphysics, *J. Geophys. Res.*, 114, D04205,
 505 doi:10.1029/2008JD010782, 2009.

506 Feingold, G., Kreidenweis, S. M., Stevens, B., and Cotton, W. R.: Numerical simulation of
 507 stratocumulus processing of cloud condensation nuclei through collision-coalescence, *J.*
 508 *Geophys. Res.*, 101, 21,391-21,402, 1996.

509 Fridlind, A. M., van Didenhoven, B., Ackerman, A. S., Avramov, A., Mrowiec, A.,
 510 Morrison, H., Zuidema, P., and Shupe, M. D.: A FIRE-ACE/SHEBA case study of
 511 mixed-phase Arctic boundary-layer clouds: Entrainment rate limitations on rapid
 512 primary ice nucleation processes, *J. Atmos. Sci.*, 69, 365-389, doi:10.1175/JAS-D-11-
 513 052.1, 2012.

514 Hobbs, P. V. and Rangno A. L.: Microstructure of low and middle- level clouds over the
 515 Beaufort Sea, *Q. J. Roy. Meteor. Soc.*, 124, 2035-2071, 1998.

516 Hoose, C. and Möhler, O.: Heterogeneous ice nucleation on atmospheric aerosols: a review
 517 of results from laboratory experiments, *Atmos. Chem. Phys.*, 12, 9817-9854,
 518 doi:10.5194/acp-12-9817-2012, 2012.

519 Iacono, M. J., Delamere, J. S., Mlawer, E. J., Shephard, M. W., Clough, S. A., and Collins,
 520 W. D.: Radiative forcing by long-lived greenhouse gases: Calculations with the AER

521 Radiative transfer models, *J. Geophys. Res.*, 113, D13103, doi:10.1029/2008JD009944,
 522 2008.

523 Intrieri, J. M., Fairall, C. W., Shupe, M. D., Persson, P. O. G., Andreas, E., Guest, P. S., and
 524 Moritz, R. E.: An annual cycle of Arctic surface cloud forcing at SHEBA, *J. Geophys.*
 525 *Res.*, 107, 8039, doi:10.1029/2000JC000439, 2002.

526 Kanji, Z., DeMott, P., Möhler, O., and Abbatt, J.: Results from the University of Toronto
 527 continuous flow diffusion chamber at ICIS 2007: instrument intercomparison and ice
 528 onsets for different aerosol types, *Atmos. Chem. Phys.*, 11:31-41, doi:10.5194/acp-11-
 529 31-2011, 2011.

530 Karlsson, J. and Svensson, G.: The simulation of Arctic clouds and their influence on the
 531 winter surface temperature in present-day climate in the CMIP3 multi-model dataset,
 532 *Clim. Dynam.*, 36, 623–635, 2011.

533 Klein, S. A., McCoy, R., Morrison, H., Ackerman, A., Avramov, A., de Boer, G., Chen, M.,
 534 Cole, J., DelGenio, A. D., Falk, M., Foster, M., Fridlind, A., Golaz, J.-C., Hashino, T.,
 535 Harrington, J., Hoose, C., Khairoutdinov, M., Larson, V., Liu, X., Luo, Y., McFarquhar,
 536 G., Menon, S., Neggers, R., Park, S., von Salzen, K., Schmidt, J. M., Sednev, I.,
 537 Shipway, B., Shupe, M., Spangenberg, D., Sud, Y., Turner, D., Veron, D., Walker, G.,
 538 Wang, Z., Wolf, A., Xie, S., Xu, K.-M., Yang, G., and Zhang, G.: Intercomparison of
 539 model simulations of mixed-phase clouds observed during the ARM Mixed-Phase Arctic
 540 Cloud Experiment. I: Single-layer cloud, *Q. J. Roy. Meteor. Soc.*, 135, 979–1002, 2009.

541 Korolev, A.: Limitations of the Wegener–Bergeron–Findeisen mechanism in the evolution of
 542 mixed-phase clouds, *J. Atmos. Sci.*, 64, 3372–3375, doi:10.1175/JAS4035.1, 2007.

543 Korolev, A. and Sussman, B.: A technique for habit classification of cloud particles, *J. Atmos.*
 544 *Oceanic Technol.*, 17, 1048–1057, 2000.

545 Kulkarni, G., Fan, J., Comstock, J., Liu, X., and Ovchinnikov, M.: Laboratory measurements
 546 and model sensitivity studies of dust deposition ice nucleation, *Atmos. Chem. Phys.*,
 547 12:7295-7308, doi:10.5194/acp-12-7295-2012, 2012.

548 Levin, Z. and Yankofsky, S.: Contact versus immersion freezing of freely suspended droplets
 549 by bacterial ice nuclei, *J. Appl. Meteorol. Clim.*, 22, 1964-1966, 1983.

550 Lilly, D. K.: Models of cloud-topped mixed layers under a strong inversion, *Q. J. Roy.*
 551 *Meteor. Soc.*, 94, 292–309, 1968.

552 Lüönd, F., Stetzer, O., Welti, A., and Lohmann, U.: Experimental study on ice nucleation
 553 ability of size selected kaolinite particles in the immersion mode, *J. Geophys. Res.*,
 554 115:D14201, doi:10.1029/2009JD012959, 2010.

555 McFarquhar, G. M., Zhang, G., Poellot, M. R., Kok, G. L., McCoy, R., Tooman, T., Fridlind,
 556 A., and Heymsfield, A. J.: Ice properties of single-layer stratocumulus during the Mixed-
 557 Phase Arctic Cloud Experiment: 1. Observations, *J. Geophys. Res.*, 112, D24201,
 558 doi:10.1029/2007JD008633, 2007.

559 McFarquhar, G. M., Ghan, S., Verlinde, J., Korolev, A., Strapp, J. W., Schmid, B.,
 560 Tomlinson, J. M., Wolde, M., Brooks, S. D., Cziczo, D., Dubey, M. K., Fan, J., Flynn,
 561 C., Gultepe, I., Hubbe, J., Gilles, M. K., Laskin, A., Lawson, P., Leaitch, W. R., Liu, P.,
 562 Liu, X., Lubin, D., Mazzoleni, C., Macdonald, A.-M., Moffet, R. C., Morrison, H.,
 563 Ovchinnikov, M., Shupe, M. D., Turner, D. D., Xie, S., Zelenyuk, A., Bae, K., Freer, M.,
 564 and Glen, A.: Indirect and Semi-Direct Aerosol Campaign (ISDAC): The Impact of

565 Arctic Aerosols on Clouds, B. Am. Meteorol. Soc., 92, 183–201,
 566 doi:10.1175/2010BAMS2935.1, 2011.

567 Möhler, O., Büttner, S., Linke, C., Schnaiter, M., Saathoff, H., Stetzer, O., Wagner, R.,
 568 Krämer, M., Mangold, A., Ebert, V., and Schurath, U.: Effect of sulfuric acid coating on
 569 heterogeneous ice nucleation by soot aerosol particles, J. Geophys. Res., 110:D11210,
 570 doi: 10.1029/2004JD005169, 2005.

571 Möhler, O., Field, P., Connolly, P., Benz, S., Saathoff, H., Schnaiter, M., Wagner, R., Cotton,
 572 R., Krämer, M., Mangold, A., and Heymsfield, A.: Efficiency of the deposition mode ice
 573 nucleation on mineral dust particles, Atmos. Chem. Phys., 6:3007-3021,
 574 doi:10.5194/acp-6-3007-2006, 2006.

575 Morrison, H. and Pinto, J. O.: Mesoscale modeling of springtime Arctic mixed-phase
 576 stratiform clouds using a new two-moment bulk microphysics scheme, J. Atmos. Sci., 62,
 577 3683-3704, 2005.

578 Morrison, H., Thompson, G., and Tatarskii, V.: Impact of cloud microphysics on the
 579 development of trailing stratiform precipitation in a simulated squall line: Comparison of
 580 one- and two-moment schemes, Mon. Wea. Rev., 137, 991-1007,
 581 doi:10.1175/2008MWR2556.1, 2009.

582 Paulson, C. A.: The mathematical representation of wind speed and temperature profiles in
 583 the unstable atmospheric surface layer, J. Appl. Meteor., 9, 857–861, 1970.

584 Persson, P. O. G.: Onset and end of the summer melt season over sea ice: Thermal structure
 585 and surface energy perspective from SHEBA, Clim. Dynam., 39, 1349-1371,
 586 doi:10.1007/s00382-011-1196-9, 2012.

587 Pinti, V., Marcolli, C., Zobrist, B., Hoyle, C., and Peter, T.: Ice nucleation efficiency of clay
 588 minerals in the immersion mode, *Atmos. Chem. Phys.*, 12:5859-5878, doi:10.5194/acp-
 589 12-5859-2012, 2012.

590 Pruppacher, H. and Klett, J.: *Microphysics of clouds and precipitation*. Kluwer Academic
 591 Publishers, 2nd edition, 1997.

592 Roberts, P. and Hallett, J.: A laboratory study of the ice nucleating properties of some
 593 mineral particulates, *Q. J. R. Meteorol. Soc.*, 94, 25 – 34, 1967.

594 Sandvik, A., Biryulina, M., Kvamsto, N., Stamnes, J., and Stamnes, K.: Observed and
 595 simulated microphysical composition of Arctic clouds: Data properties and model
 596 validation, *J. Geophys. Res.* 112, D05205, 2007.

597 Sedlar, J., Shupe, M. D., and Tjernström, M.: On the relationship between thermodynamic
 598 structure, cloud top, and climate significance in the Arctic, *J. Climate*, 25, 2374–2393,
 599 2012.

600 Sedlar, J., Tjernström, M., Mauritsen, T., Shupe, M. D., Brooks, I. M., Persson, P. O. G.,
 601 Birch, C. E., and C. Leck, C.: A transitioning Arctic surface energy budget: The impacts
 602 of solar zenith angle, surface albedo and cloud radiative forcing, *Clim. Dynam.*, 37,
 603 1643–1660, doi:10.1007/s00382-010-0937-5, 2011.

604 Serreze, M. C., Barrett, A. P., and Stroeve, J.: Recent changes in tropospheric water vapor
 605 over the Arctic as assessed from radiosondes and atmospheric reanalyses. *J. Geophys.*
 606 *Res.*, 117, D10104, doi:10.1029/2011JD017421, 2012.

607 Sheridan, L. M., Harrington, J. Y., Lamb, D., and Sulia, K.: Influence of ice crystal aspect
 608 ratio on the evolution of ice size spectra during vapor depositional growth, *J. Atmos. Sci.*,
 609 66, 3732–3743, doi:10.1175/2009JAS3113.1, 2009.

610 Shupe, M. D.: A ground-based multiple remote-sensor cloud phase classifier, *Geophys. Res.*
 611 *Lett.*, 34, L2209, doi:10.1029/2007GL031008, 2007.

612 Shupe, M. D and J. M. Intrieri: Cloud radiative forcing of the Arctic surface: The influence
 613 of cloud properties, surface albedo, and solar zenith angle, *J. Climate*, 17, 616-628, 2004.

614 Shupe, M. D, Matrosov, S. Y., and Uttal, T.: Arctic mixed phase cloud properties derived
 615 from surface-based sensors at SHEBA, *J. Atmos. Sci.*, 63, 697-811, 2006.

616 Shupe, M. D, Persson, P. O. G., Brooks, I. M., Tjernström, M., Sedlar, J., Mauritsen, T.,
 617 Sjogren, S., and Leck, C.: Cloud and boundary layer interactions over the Arctic sea-ice
 618 in late summer, *Atmos. Chem. Phys.*, 13, 9379-9400, 2013.

619 Skamarock, W. C., Klemp, J. B., Dudhia, J., Gill, D. O., Barker, D. M., Duda, M. G., Huang,
 620 X.-Y., Wang, W., and Powers, J. G.: A description of the Advanced Research WRF
 621 version 3, NCAR Tech. Note NCAR/TN-475+STR, 113 pp., 2008.

622 Solomon, A., Morrison, H., Persson, P. O. G., Shupe, M. D., and Bao, J.-W.: Investigation of
 623 microphysical parameterizations of snow and ice in Arctic clouds during M-PACE
 624 through model-observation comparisons, *Mon. Wea. Rev.*, 137, 3110-3128,
 625 doi:10.1175/2009MWR2688.1, 2009.

626 Solomon, A., Shupe, M. D., Persson, P. O. G., and Morrison, H.: Moisture and dynamical
 627 interactions maintaining decoupled Arctic mixed-phase stratocumulus in the presence of
 628 a humidity inversion, *Atmos. Chem. Phys.*, 11, 10127-10148, doi:10.5194/acp-11-10127-
 629 2011, 2011.

630 Solomon, A., Shupe, M. D., Persson, P. O. G., Morrison, H., Yamaguchi, T., Caldwell, P. M.,
 631 and de Boer, G.: The sensitivity of springtime Arctic mixed-phase stratocumulus clouds

632 to surface layer and cloud-top inversion layer moisture sources, *J. Atmos. Sci.*, 71, 574-
633 595, doi:10.1175/JAS-D-13-0179.1, 2014.

634 Tjernström, M., Sedlar, J., and Shupe, M. D.: How well do regional climate models
635 reproduce radiation and clouds in the Arctic? An evaluation of ARCMIP simulations, *J.*
636 *Appl. Met. Clim.*, 47, 2405–2422, 2008.

637 Tjernström, M., C. Leck, C., Persson, P. O. G., Jensen, M. L., Oncley, S. P., and Targino, A.:
638 The summertime Arctic atmosphere: Meteorological measurements during the Arctic
639 Ocean Experiment 2001, *B. Am. Meteorol. Soc.*, 85, 1305–1321, 2004.

640 Turner, D. D., Clough, S. A., Liljegren, J. C., Clothiaux, E. E., Cady-Pereira, K., and Gaustad,
641 K. L.: Retrieving precipitable water vapor and liquid water path from Atmospheric
642 Radiation Measurement (ARM) program’s microwave radiometers, *IEEE T. Geosci.*
643 *Remote*, 45, 3680–3690, 2007.

644 Verlinde, J., Harrington, J. Y., McFarquhar, G. M., et al.: The Mixed-Phase Arctic Cloud
645 Experiment (M-PACE), *B. Am. Meteorol. Soc.*, 88, 205–221, doi:10.1175/BAMS-88-2-
646 205, 2007.

647 Walsh, J. E. and Chapman, W. L.: Arctic cloud-radiation temperature associations in
648 observational data and atmospheric reanalyses, *J. Climate*, 11, 3030–3045, 1998.

649 Webb, E. K.: Profile relationships: The log-linear range, and extension to strong stability.
650 *Quart. J. Roy. Meteor. Soc.*, 96, 67–90, 1970.

651 Wise, M., Baustian, K., Koop, T., Freedman, M., Jensen, E., and Tolbert, M.: Depositional
652 ice nucleation onto crystalline hydrated nacl particles: a new mechanism for ice
653 formation in the troposphere, *Atmos. Chem. Phys.*, 12:1121-1134, doi:10.5194/acp-12-
654 1121-2012, 2012.

655 Yamaguchi, T. and Feingold, G.: Technical note: Large-eddy simulation of cloudy boundary
656 layer with the Advanced Research WRF model, J. Adv. Model. Earth Syst., 4, M09003,
657 doi:10.1029/2012MS000164, 2012.

Figure Captions

Figure 1: Sounding measured at 17:34 UTC 8 April 2008 at Barrow, Alaska (71.338N, 156.68W). Left) Water vapor mixing ratio (q_v), temperature (T), and potential temperature (Theta), in units of g kg^{-1} , degrees Kelvin, and degrees Kelvin respectively. Right) Zonal wind (U) and meridional wind (V), in units of m s^{-1} . Gray shading marks the extent of the cloud layer. The dashed lines show the initial profiles used in the WRFLES experiments. The dashed line overlaying water vapor mixing ratio is the initial profile for the total water mixing ratio.

Figure 2: IN number concentration active at water saturation vs. temperature based on the empirical relationship derived in DeMott et al. (2010) (blue line) used to initialize IN number concentration in each bin. Black vertical lines indicate threshold temperatures for nucleation in the 16 IN bins. IN increments between lines indicate the additional IN available for nucleation at colder temperatures.

Figure 3: Sensitivity of ice water path to the parameter F in equation (2). Note the similar ice water paths for $F=4$ and $F=6$ (total N_{IN} initial values 5.8 and 8.7 L^{-1} , respectively).

Figure 4: A,B,D) Sensitivity of LWP and IWP to snow density and fall speeds. LWP shown with solid lines and IWP shown with dashed lines, in units of g m^{-2} . C) Fall speeds used in sensitivity studies, in units of m s^{-1} . A) Sensitivity to reducing snow density from 100 kg m^{-3} to 50 kg m^{-3} (red lines) using Control (CNT) fall speeds (red line in C). B) Sensitivity to reducing snow fall speeds (green line in C) using Control snow density (red lines). D) Sensitivity to increasing snow fall speeds (blue line in C) using Control snow density (red lines).

680 **Figure 5:** Simulated ice particle number size distributions using in-cloud mass and number
681 concentrations. Ice water mixing ratio = $3\text{e-}4$ g/kg, ice number concentration = $0.4/\text{L}$, snow
682 water mixing ratio = $2.4\text{e-}2$ g/kg, snow number concentration = $0.45/\text{L}$.

683 **Figure 6:** (A) N_{IN} and (B) N_{ICE} averaged over 0.5 hours at hour 20, in units of $\text{L}^{-1} \text{hr}^{-1}$. Grey
684 shading indicates the extent of the cloud layer. Green dash lines indicate the top and bottom
685 of the mixed layer.

686 **Figure 7:** Time-height cross sections of horizontally-averaged (A) IN advection plus
687 subsidence, in units of $\text{L}^{-1}\text{hour}^{-1}$, (B) ice plus snow number concentration, in units of L^{-1} , (C)
688 water vapor mixing ratio, in units of g kg^{-1} , and (D) relative humidity with respect to ice, in
689 units of percent, from CNT simulation. Temperature, in units of $^{\circ}\text{C}$, shown with black
690 contour lines in (B,C,D).

691 **Figure 8:** Control and NoRecycle time series for hours 6-40 (smoothed with 90 minute
692 running average). NoRecycle shown with red and black dashed lines. A) LWP (black) and
693 IWP (red), in units of g m^{-2} . B) Minimum horizontally-averaged temperature in the column,
694 in units of $^{\circ}\text{C}$. C) Mixed-layer depth (blue), top height (red), and base height (black), in units
695 of km. D) N_{ICE} integrated over cloud layer (referred to as CL, red) and N_{IN} integrated over
696 subcloud layer (referred to as SubCL, black), in units of m L^{-1} (i.e., meters/liter).

697 **Figure 9:** Horizontally-averaged fluxes from Control and NoRecycle integrations for hours
698 6-40 (smoothed with 90 minute running average). NoRecycle shown with red and black
699 dashed lines. A) N_{ICE} flux at cloud base due to turbulence+subsidence+precipitation (red),
700 mixed-layer base due to turbulence+subsidence+precipitation (black), and due to activation
701 (multiplied by -1, blue), in units of $\text{m L}^{-1} \text{hr}^{-1}$. B) N_{IN} flux at cloud base due to turbulence

702 (red), N_{IN} flux due to sublimation (black), and precipitation of N_{ICE} at cloud base (multiplied
 703 by -1, blue), in units of $\text{m L}^{-1} \text{ hr}^{-1}$. C) N_{IN} entrainment at mixed-layer top (red) and base
 704 (black), in units of $\text{m L}^{-1} \text{ hr}^{-1}$.

705 **Figure 10:** Schematic of feedback loops that maintain ice production and the phase-
 706 partitioning between cloud liquid and ice in an AMPS. Red colors denote N_{IN} . Blue colors
 707 denote N_{ICE} . The size of the arrow indicates the relative magnitude of the flux. Vertical
 708 profiles of N_{ICE} , N_{IN} , relative humidity, and temperature shown with thin blue, red, green, and
 709 yellow lines, respectively.

710 **Figure 11:** A) LWP (black) and IWP (red), in units of g m^{-2} . (B) Downward surface
 711 shortwave radiation and turbulent kinetic energy (TKE) at cloud base, in units of Wm^{-2} and
 712 m^2s^{-2} , respectively. C) N_{ICE} in cloud layer (referred to as CL, red) and N_{IN} in subcloud layer
 713 (referred to as SubCL, black), in units of m L^{-1} . (D) Total, turbulent, precipitation N_{ICE} flux at
 714 cloud base (referred to as CL base, red, green, blue, respectively) and total N_{ICE} flux at
 715 mixed-layer base (referred to as ML base, black), in units of $\text{m L}^{-1} \text{ hr}^{-1}$, for the SW
 716 integration for hours 16-76. Grey shading indicates hours with zero downwelling surface
 717 shortwave radiation. E) N_{IN} entrainment at mixed-layer top (red) and base (black), in units of
 718 $\text{m L}^{-1} \text{ hr}^{-1}$. (F) N_{IN} flux at cloud base due to turbulence (red), N_{IN} flux due to sublimation
 719 (black), and activation of N_{ICE} (blue), in units of $\text{m L}^{-1} \text{ hr}^{-1}$.

720 **Figure 12:** A) Phase diagram of TKE at cloud base vs. N_{ICE} in the cloud layer starting at
 721 peak shortwave hour 40, in units of m L^{-1} and $\text{m L}^{-1} \text{ hr}^{-1}$, respectively. Colors show
 722 sublimation in units of $\text{m L}^{-1} \text{ hr}^{-1}$. H) 24-hour phase diagrams of sublimation vs. minimum
 723 relative humidity in the subcloud layer starting at peak shortwave hour 40, in units of m L^{-1}

724 hr^{-1} and %, respectively. Colors show total N_{ICE} flux at cloud base, $\text{m L}^{-1} \text{hr}^{-1}$. Hours 42-47,
725 47-50, 50-56, and 57-62 indicated with green, blue, black, red arrows, respectively.
726 Minimum shortwave indicated with the moon symbol. Maximum shortwave indicated with
727 the sun symbol.

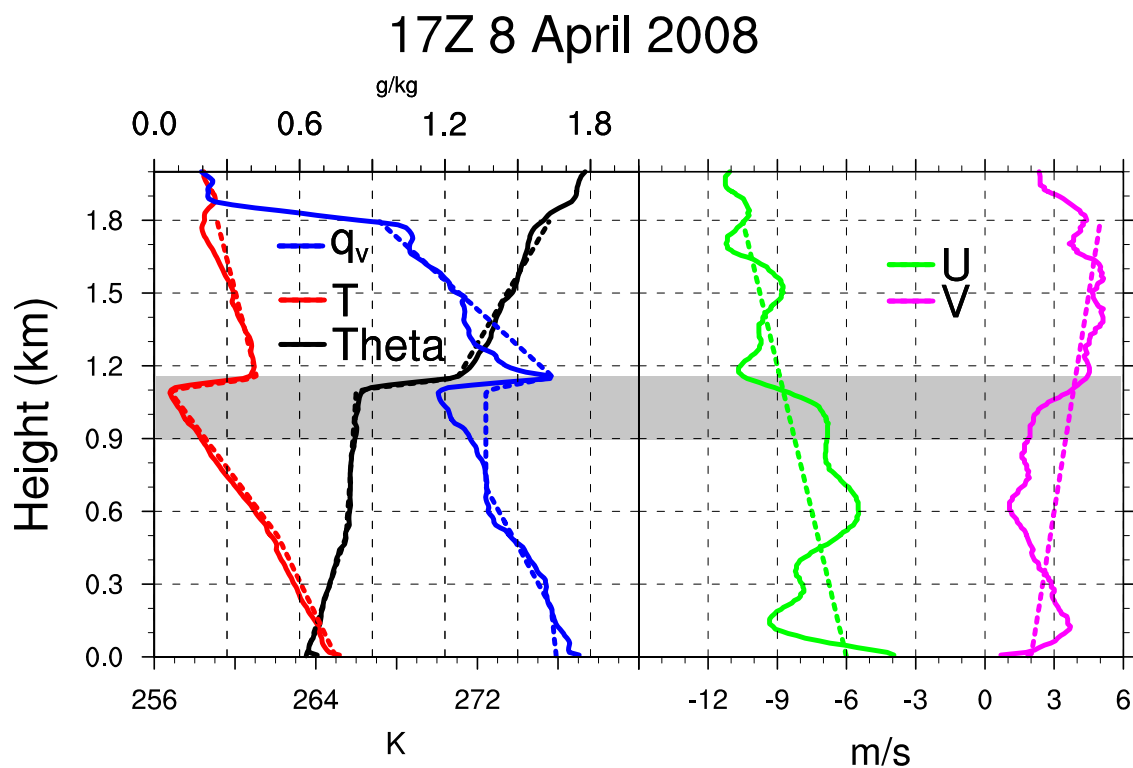
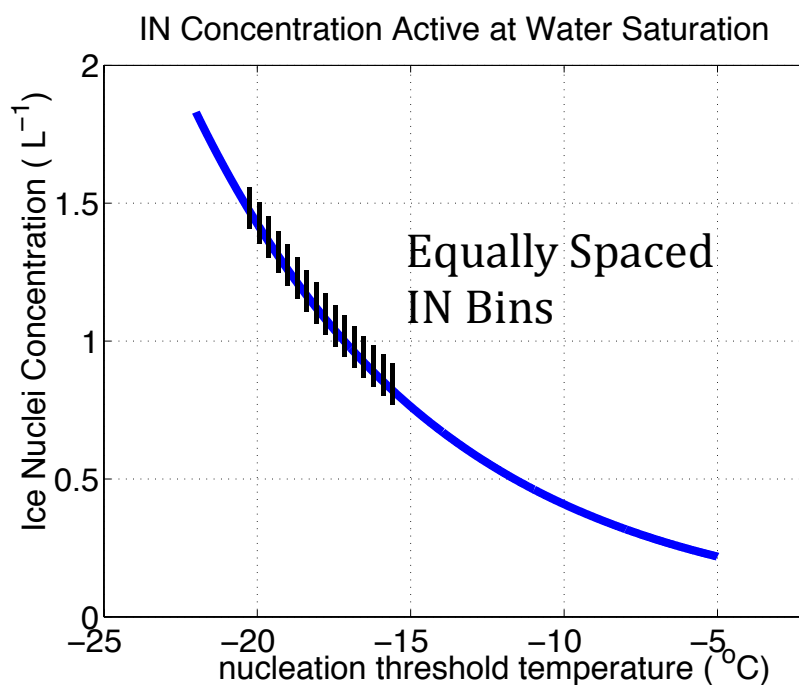


Figure 1: Sounding measured at 17:34 UTC 8 April 2008 at Barrow, Alaska (71.338N, 156.68W). Left) Water vapor mixing ratio (q_v), temperature (T), and potential temperature (Θ), in units of g kg^{-1} , degrees Kelvin, and degrees Kelvin respectively. Right) Zonal wind (U) and meridional wind (V), in units of m s^{-1} . Gray shading marks the extent of the cloud layer. The dashed lines show the initial profiles used in the WRFLES experiments. The dashed line overlaying water vapor mixing ratio is the initial profile for the total water mixing ratio.

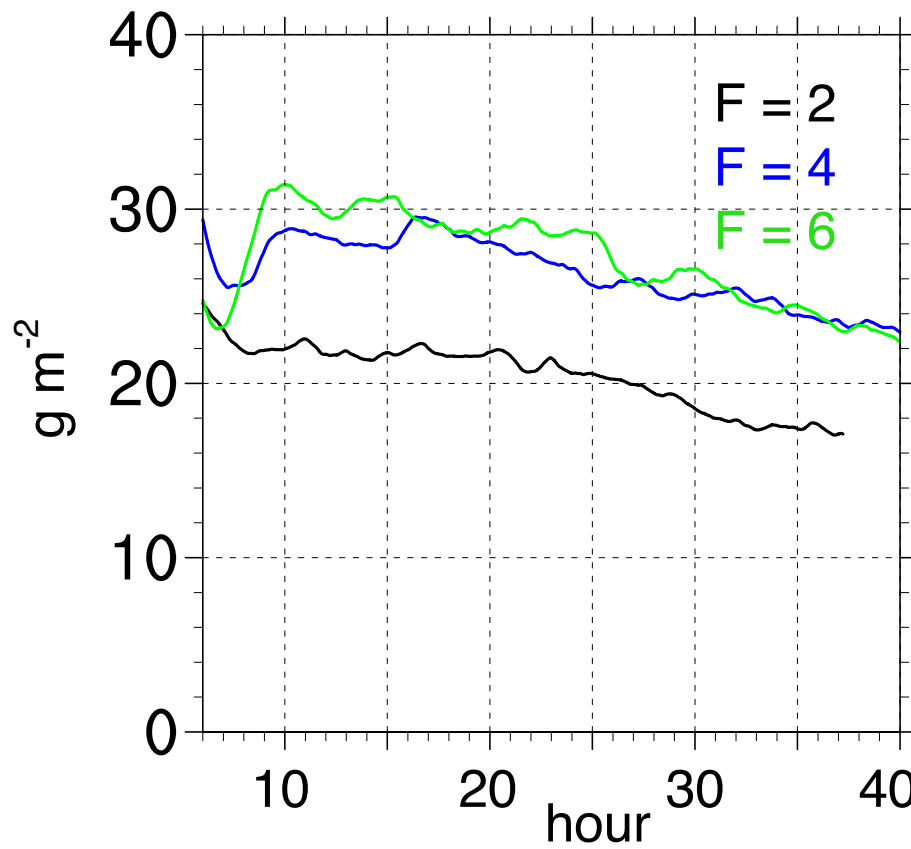
735



736
737

738 **Figure 2:** IN number concentration active at water saturation vs. temperature based on the
 739 empirical relationship derived in DeMott et al. (2010) (blue line) used to initialize IN number
 740 concentration in each bin. Black vertical lines indicate threshold temperatures for nucleation
 741 in the 16 IN bins. Note additional IN become available for nucleation at colder temperatures,
 742 such that, for example, at $-20.2^{\circ}C$ (the coldest temperature in the Control simulation) the total
 743 number of IN available for activation is $\sim 1.5 L^{-1}$.

Ice Water Paths



744

745 **Figure 3:** Sensitivity of ice water path to the parameter F in equation (2). Note the similar ice

746 water paths for $F=4$ and $F=6$ (total N_{IN} initial values of 5.8 and 8.7 L^{-1} , respectively).

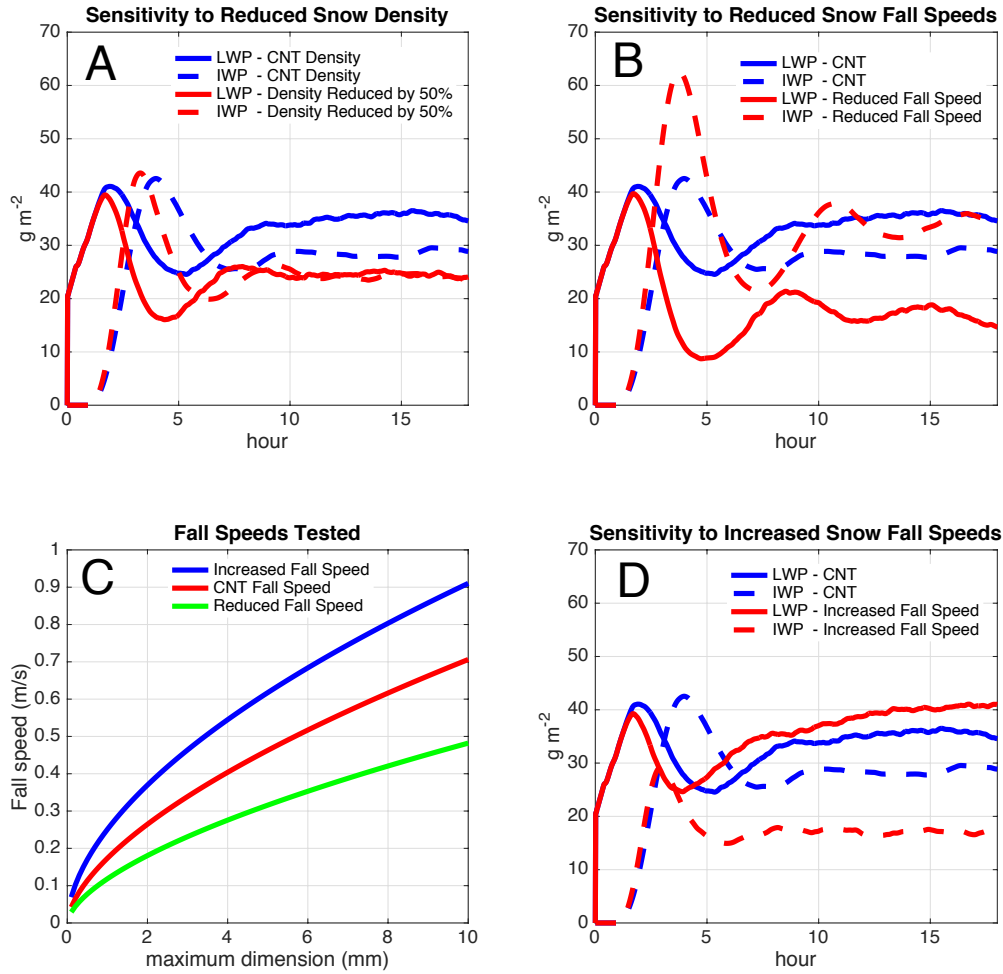


Figure 4: A,B,D) Sensitivity of LWP and IWP to snow density and fall speeds. LWP shown with solid lines and IWP shown with dashed lines, in units of $g\ m^{-2}$. C) Fall speeds used in sensitivity studies, in units of $m\ s^{-1}$. A) Sensitivity to reducing snow density from $100\ kg\ m^{-3}$ to $50\ kg\ m^{-3}$ (red lines) using Control (CNT) fall speeds (red line in C). B) Sensitivity to reducing snow fall speeds (green line in C) using Control snow density (red lines). D) Sensitivity to increasing snow fall speeds (blue line in C) using Control snow density (red lines).

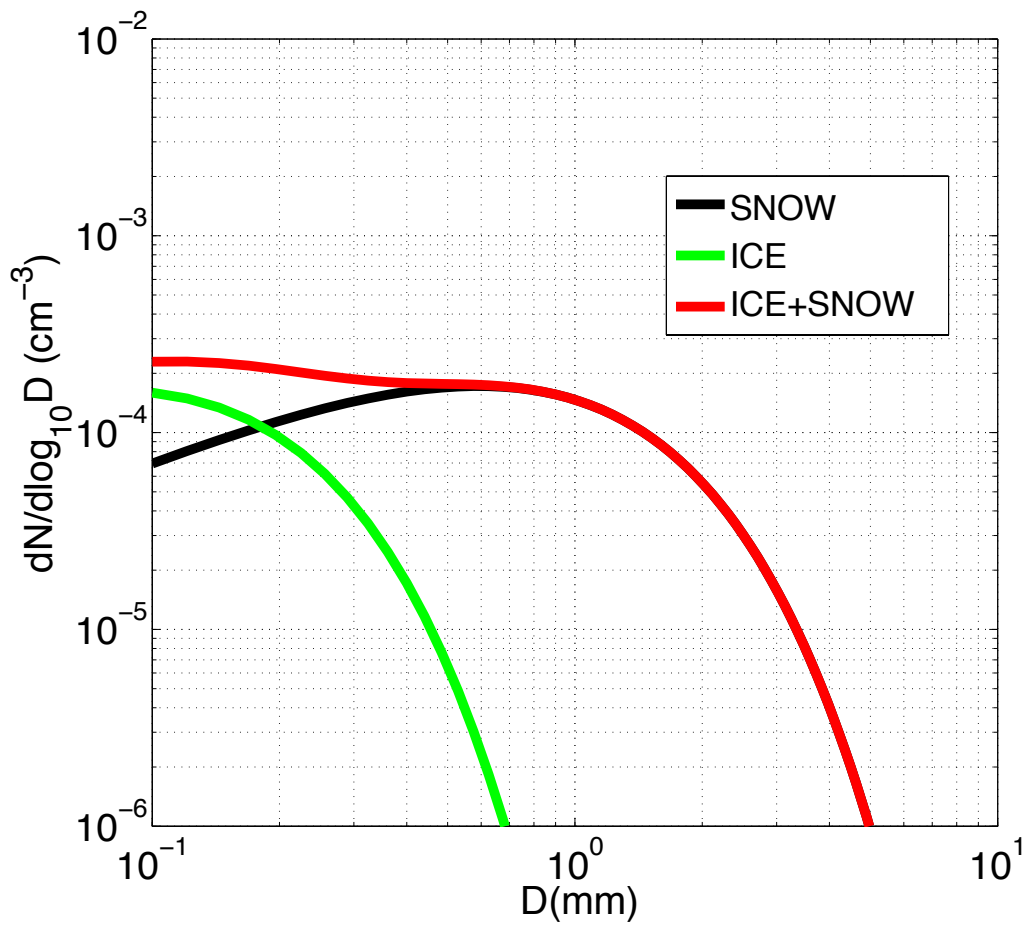
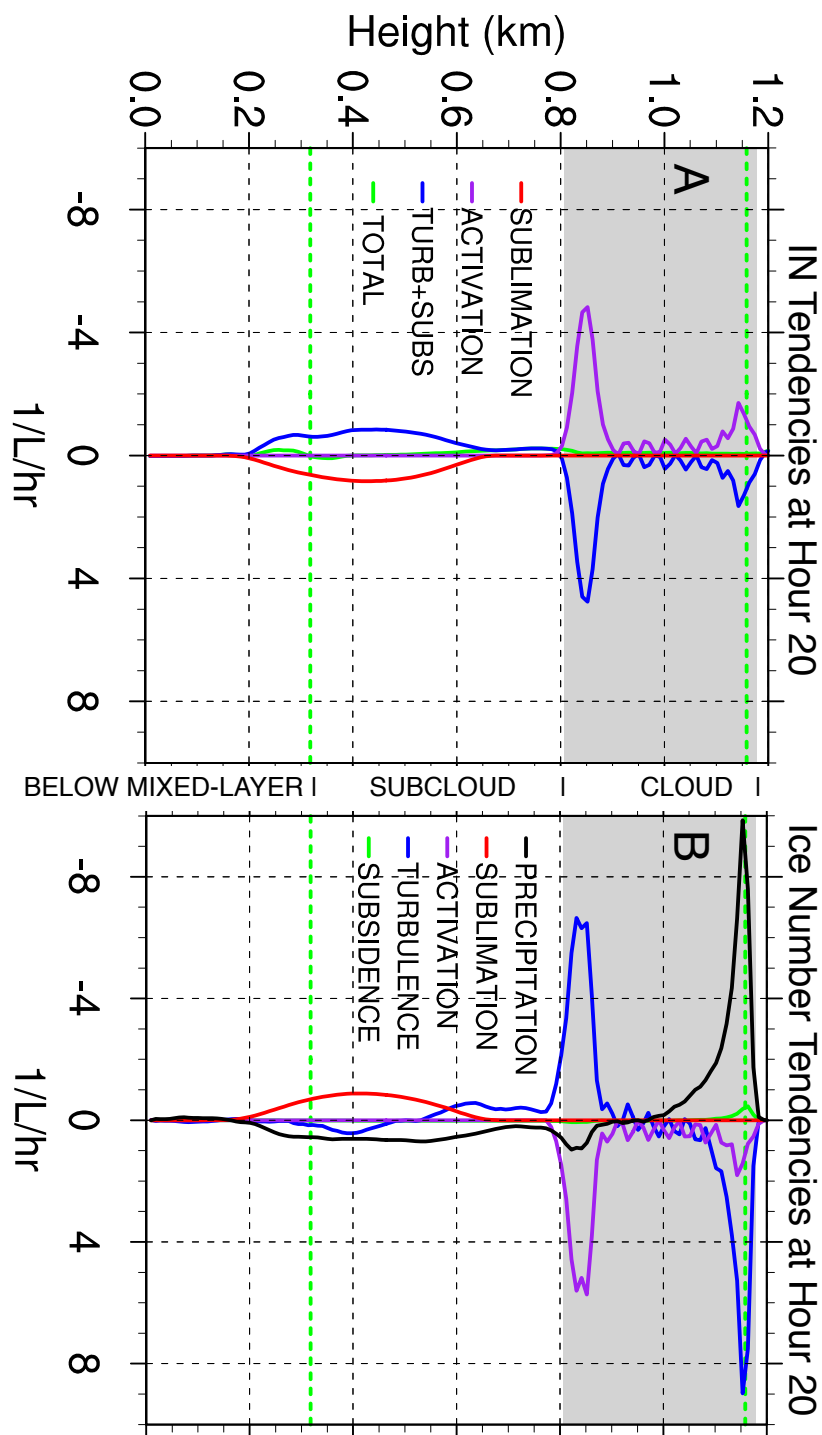


Figure 5: Simulated ice particle number size distributions using in-cloud mass and number concentrations. Ice water mixing ratio = $3\text{e-}4$ g/kg, ice number concentration = $0.4/\text{L}$, snow water mixing ratio = $2.4\text{e-}2$ g/kg, snow number concentration = $0.45/\text{L}$.



761 **Figure 6:** (A) N_{IN} and (B) N_{ICE} averaged over 0.5 hours at hour 20, in units of $L^{-1} hr^{-1}$. Grey
 762 shading indicates the extent of the cloud layer. Green dash lines indicate the top and bottom
 763 of the mixed layer.

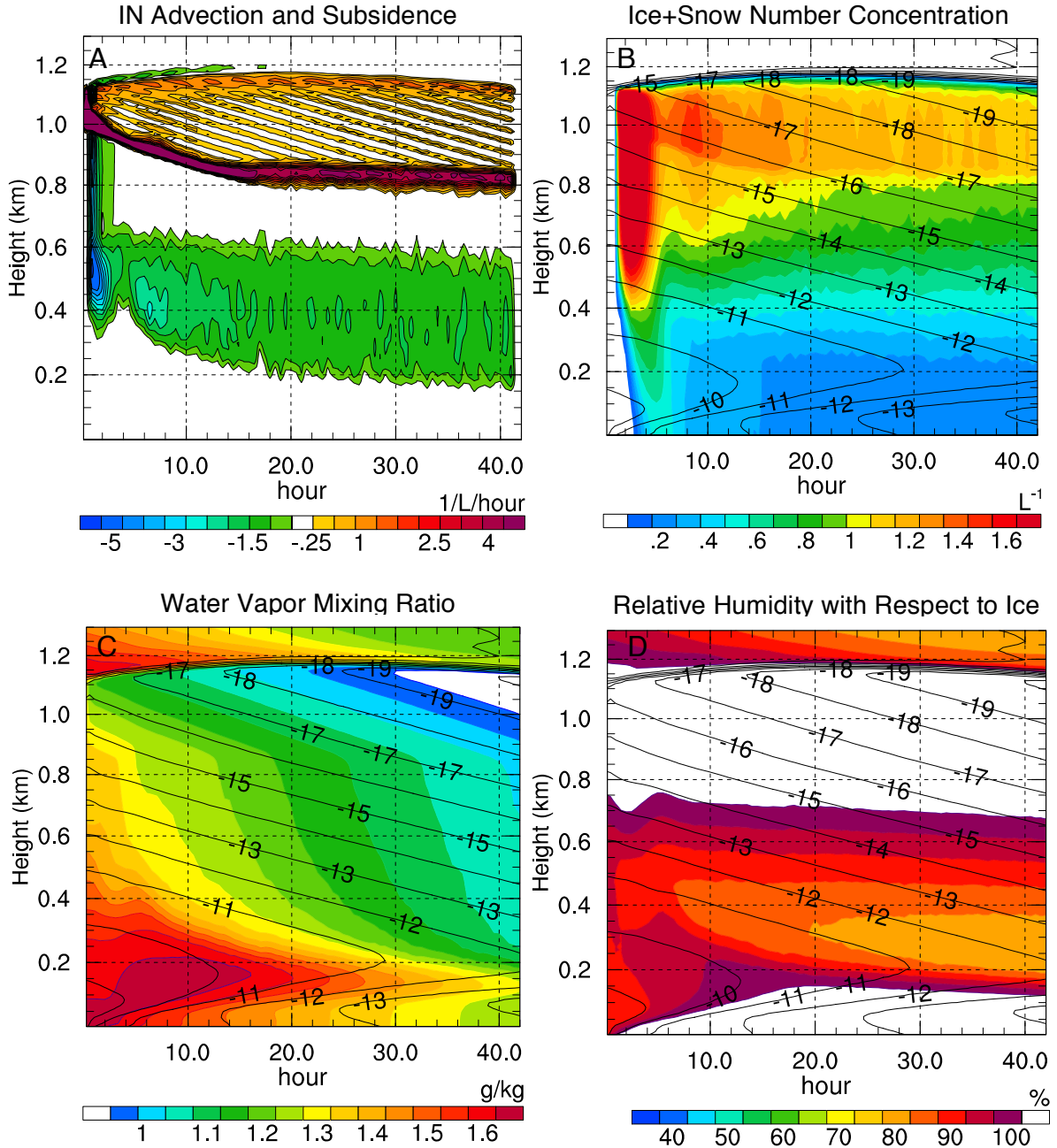
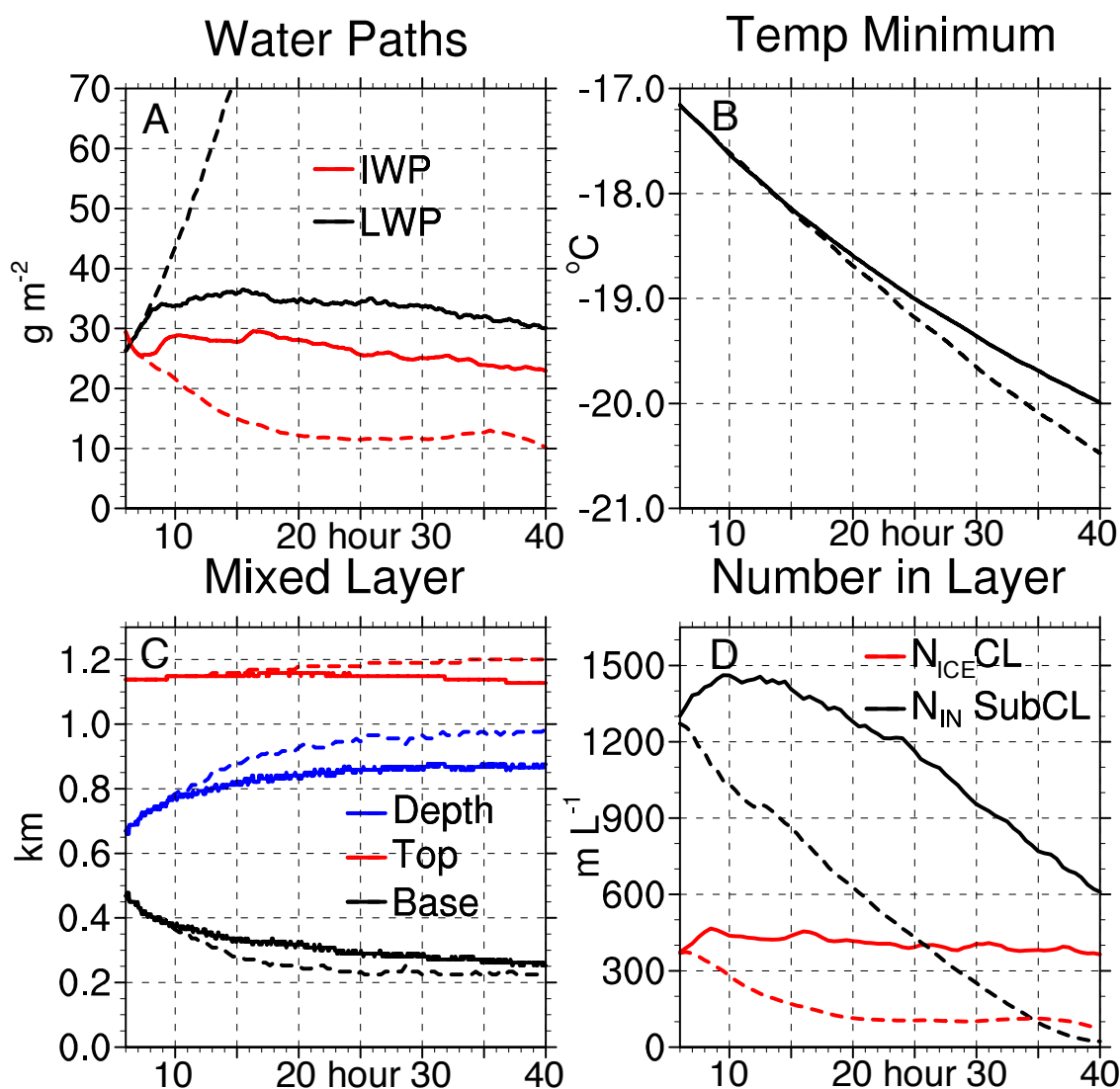
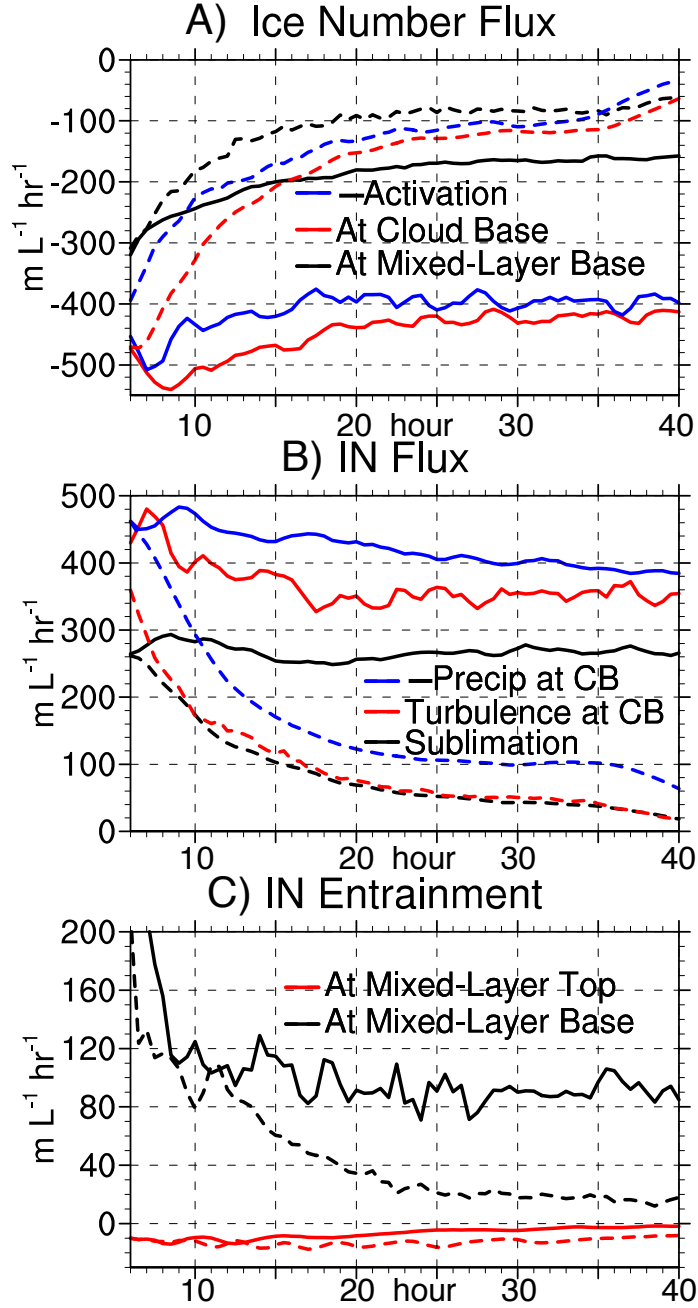


Figure 7: Time-height cross sections of horizontally-averaged (A) IN advection plus subsidence, in units of $L^{-1}hour^{-1}$, (B) ice plus snow number concentration, in units of L^{-1} , (C) water vapor mixing ratio, in units of $g\ kg^{-1}$, and (D) relative humidity with respect to ice, in units of percent, from CNT simulation. Temperature, in units of $^{\circ}C$, shown with black contour lines in (B,C,D).



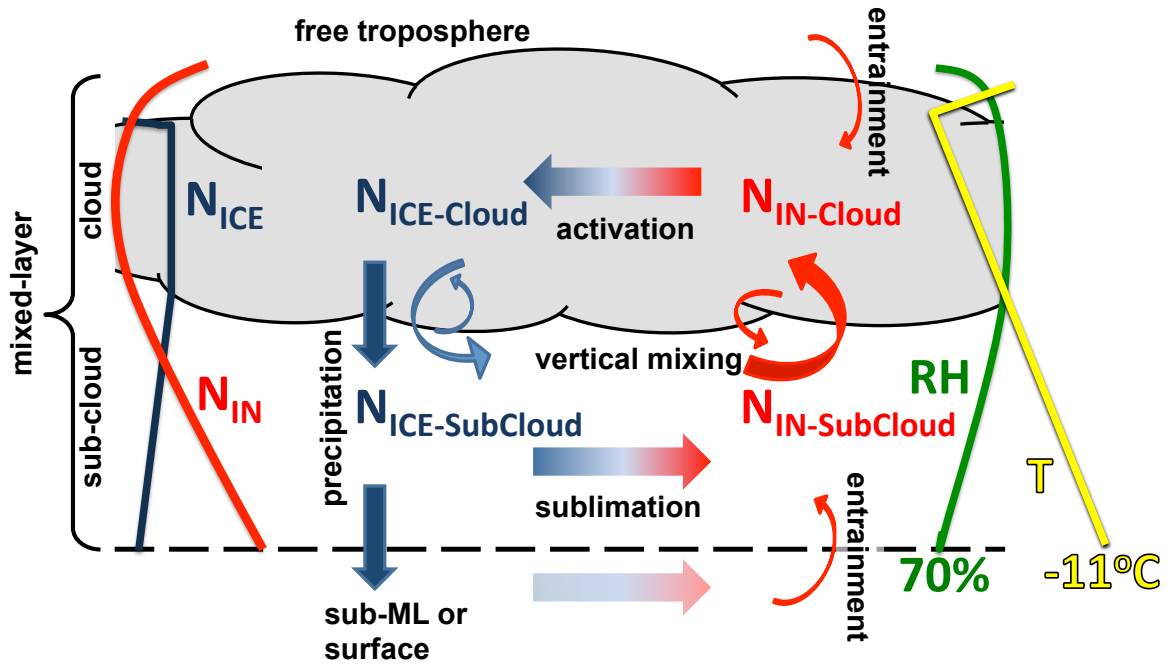
772

773 **Figure 8:** Control and NoRecycle time series for hours 6-40 (smoothed with 90 minute
 774 running average). NoRecycle shown with red and black dashed lines. A) LWP (black) and
 775 IWP (red), in units of g m^{-2} . B) Minimum horizontally-averaged temperature in the column,
 776 in units of $^{\circ}\text{C}$. C) Mixed-layer depth (blue), top height (red), and base height (black), in units
 777 of km. D) N_{ICE} integrated over cloud layer (referred to as CL, red) and N_{IN} integrated over
 778 subcloud layer (referred to as SubCL, black), in units of m L^{-1} (i.e., meters/liter).



779

780 **Figure 9:** Horizontally-averaged fluxes from Control and NoRecycle integrations for hours
 781 6-40 (smoothed with 90 minute running average). NoRecycle shown with dashed lines. A)
 782 N_{ICE} flux at cloud base due to turbulence+subsidence+precipitation (red), mixed-layer base
 783 due to turbulence+subsidence+precipitation (black), and due to activation (multiplied by -1,
 784 blue), in units of $\text{m L}^{-1} \text{ hr}^{-1}$. B) N_{IN} flux at cloud base (indicated by CB in legend) due to
 785 turbulence (red), N_{IN} flux due to sublimation (black), and precipitation of N_{ICE} at cloud base
 786 (multiplied by -1, blue), in units of $\text{m L}^{-1} \text{ hr}^{-1}$. C) N_{IN} entrainment at mixed-layer top (red)
 787 and base (black), in units of $\text{m L}^{-1} \text{ hr}^{-1}$.



788

789 **Figure 10:** Schematic of feedback loops that maintain ice production and the phase-
 790 partitioning between cloud liquid and ice in AMPS when recycling is allowed. Red colors
 791 denote N_{IN} . Blue colors denote N_{ICE} . Vertical profiles of N_{ICE} , N_{IN} , relative humidity, and
 792 temperature shown with thin blue, red, green, and yellow lines, respectively.

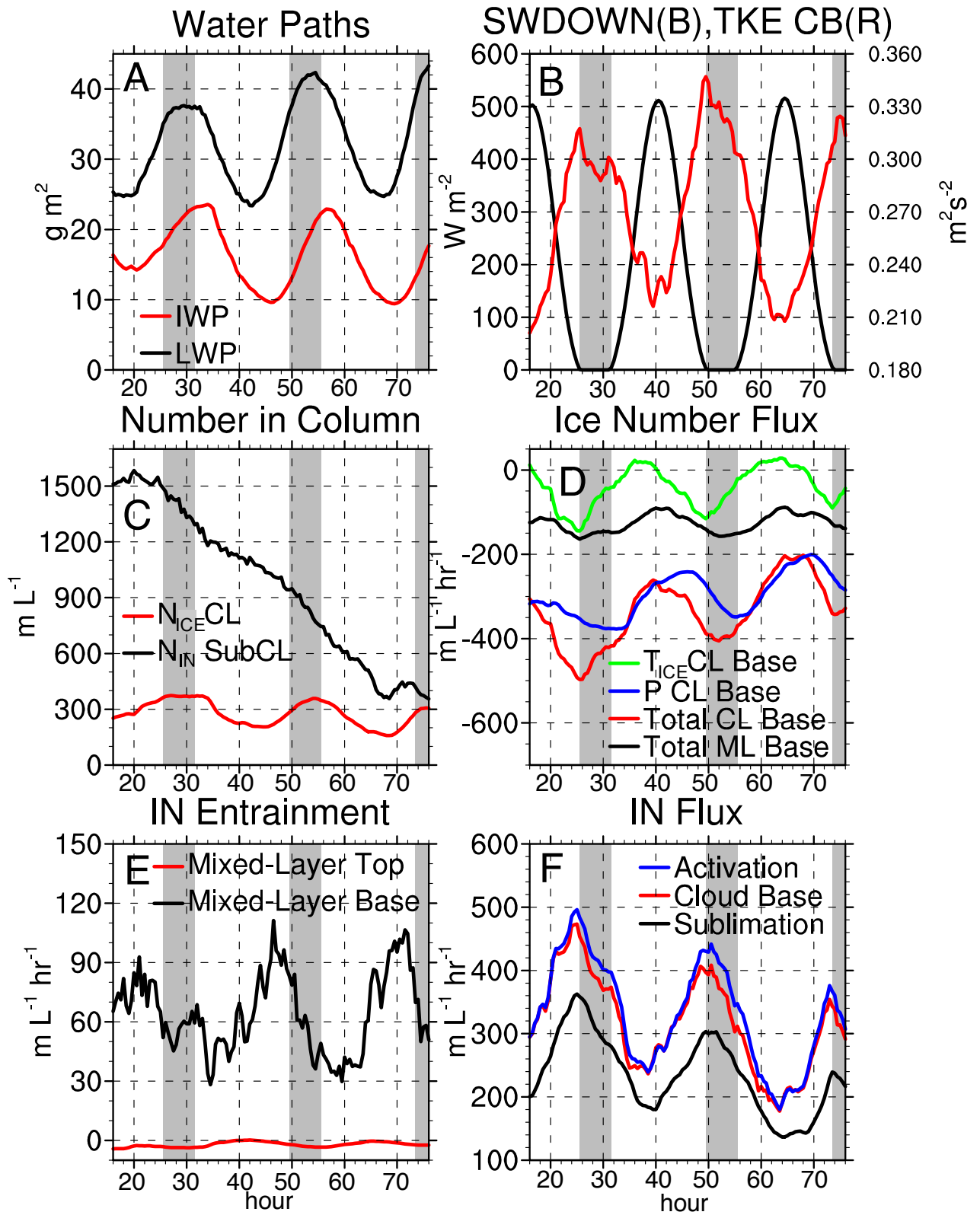
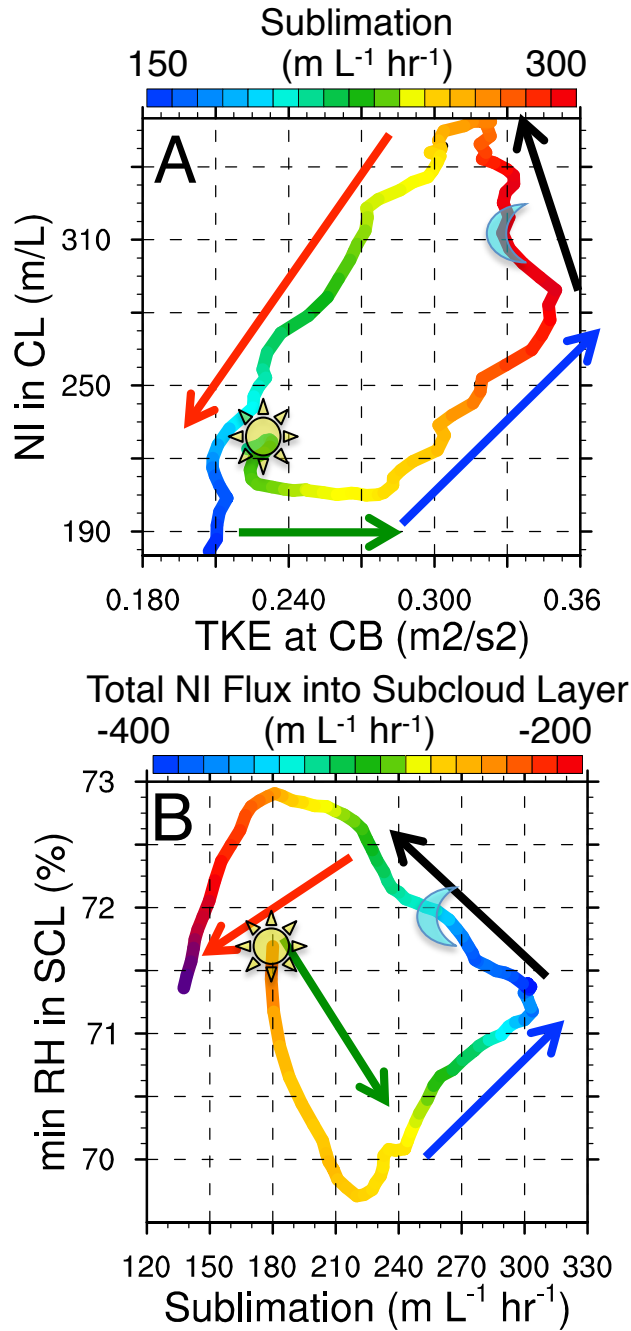


Figure 11: SW time series (see Figure captions).



795

796 **Figure 12:** A) Phase diagram of TKE at cloud base vs. N_{ICE} in the cloud layer starting at
 797 peak shortwave hour 40, in units of m L⁻¹ and m L⁻¹ hr⁻¹, respectively. Colors show
 798 sublimation in units of m L⁻¹ hr⁻¹. B) 24-hour phase diagrams of sublimation vs. minimum
 799 relative humidity in the subcloud layer starting at peak shortwave hour 40, in units of m L⁻¹
 800 hr⁻¹ and %, respectively. Colors show total N_{ICE} flux at cloud base, m L⁻¹ hr⁻¹. Hours 42-47,
 801 47-50, 50-56, and 57-62 indicated with green, blue, black, red arrows, respectively.

802 Minimum shortwave indicated with the moon symbol. Maximum shortwave indicated with
803 the sun symbol.